RHS-based Robust Hybrid Cooperative Beamforming in mmWave IoV: A Lifelong Graph Learning-based Method

Chanyuan Meng, Ke Xiong, *Member, IEEE,* Bo Gao, *Member, IEEE,* Qiang Ni, *Senior Member, IEEE,*
Pingyi Fan, *Senior Member, IEEE,* Derrick Wing Kwan Ng, *Fellow, IEEE,* Bo Ai, *Fellow, IEEE,*
and Khaled Ben Letaief, *Fellow, IEEE*

***Abstract*—As a promising candidate for next-generation reconfigurable antennas (NGRAs), the reconfigurable holographic surface (RHS) offers significant advantages in reducing hardware costs and power consumption. To enable green millimeter-wave (mmWave) Internet of Vehicles (IoV) operations in dynamic environments, this paper proposes an RHS-based robust hybrid cooperative beamforming (HCBF) transmission scheme, integrated with a machine learning (ML)-based optimization framework, to minimize the total transmit power at the base station (BS) while taking into account imperfect channel state information (CSI). First, by leveraging the unique advantages of RHS, the proposed HCBF fully exploits multi-antenna collaborative gain, thereby effectively reducing overall power consumption of the IoV system. To overcome the limitations of traditional ML-based optimization methods, which require retraining the neural network (NN) from scratch whenever the IoV network topology varies due to the dynamic entry or exit of mobile vehicles (MVs), a lifelong graph learning-based HCBF optimization method (LGL-HCBF) is developed. Specifically, in LGL-HCBF, an incremental graph convolutional network (IGCN) is employed to facilitate parameter sharing and local structural information exchange across different graph structures, thus providing stronger adaptability to dynamic variations in IoV network topology. To further address the potential stability-plasticity dilemma of LGL-HCBF, two complementary mechanisms, namely, knowledge replay and weight consolidation, are introduced to preserve the knowledge learned from previous scenarios. Simulation results demonstrate that the proposed RHS-based HCBF achieves much lower power consumption compared with traditional phased-array beamforming schemes under the same hardware-cost budget, deployment scales, and rate constraints. Moreover, the proposed LGL-HCBF exhibits faster adaptation, and superior approximation ratio, outperforming several baseline methods.**

***Index Terms*—** Reconfigurable holographic surface, IoV communications, lifelong graph learning

I. INTRODUCTION

A. Background

IT is predicted that by 2035, over one billion connected mobile vehicles (MVs) will be in operation worldwide [1], leading to rapid growth of various emerging Internet of Vehicles (IoV) applications, including autonomous driving, real-time collaboration, and in-car entertainment & information services [2]–[4]. These applications demand high data rate and low transmission latency to facilitate seamless real-time data transmission and exchange. However, the exponential increase in the number of MVs, coupled with the surge in communication demands, is exacerbating the scarcity of available spectrum resources.

To address these issues, researchers have been exploring higher frequency bands with abundant available unlicensed bandwidth, such as the millimeter-wave (mmWave) band, which can support ultra-high data rate and accommodate integration of a large number of antennas within compact devices [5], [6]. However, one of the major challenges in mmWave path propagation is the significant isotropic attenuation, as the transmission environment over mmWave frequencies is substantially more complex than that at lower-frequency bands [7]. Moreover, the high signal attenuation of the mmWave band also imposes strict limitations on the communication distance in IoV systems.

In order to mitigate the severe path loss, beamforming (BF) techniques implemented using large-scale phased antenna arrays have been demonstrated to be effective, as they enable the formation of information-carrying beams with precise directional control and substantial antenna gains [8]. Nevertheless, since each phased antenna element requires a dedicated radio-frequency (RF) chain, the hardware cost and power consumption of mmWave devices increase dramatically as the number of antenna elements grows [9]. Therefore, there is an urgent need to develop novel antenna technologies capable of substantially reducing the number of dedicated RF chains in mmWave IoVs [10].

Fortunately, the rapid development of metamaterials has spurred the emergence of innovative programmable antenna technologies [11], particularly the *reconfigurable holographic*

This work was supported in part by the National Natural Science Foundation of China (NSFC) under Grant 62571028 and 62071033, in part by the Changping Innovation Joint Fund of Beijing Natural Science Foundation under Grant L234084, and also in part by the Hong Kong Research Grant Council under the Area of Excellence (AoE) Scheme Grant No. AoE/E-601/22-R. (*Corresponding author: Ke Xiong.*)

Chanyuan Meng, Ke Xiong and Bo Gao are with School of Computer Science and Technology, Beijing Jiaotong University, Beijing 100044, China. (e-mail: {20112034, kxiong, bogao}@bjtu.edu.cn).

Qiang Ni is with the School of Computing and Communications, Lancaster University, Lancaster, LA1 4WA, U.K. (e-mail: q.ni@lancaster.ac.uk).

Pingyi Fan is with the Department of Electronic Engineering, Tsinghua University, Beijing 100084, China. (e-mail: fpy@tsinghua.edu.cn).

Derrick Wing Kwan Ng is with the School of Electrical Engineering and Telecommunications, University of New South Wales, NSW 2052, Australia (e-mail: w.k.ng@unsw.edu.au).

Bo Ai is with the School of Electronic and Information Engineering, Beijing Jiaotong University, Beijing 100044, China (e-mail: boai@bjtu.edu.cn).

Khaled Ben Letaief is with the School of Engineering, Hong Kong University of Science and Technology, Hong Kong, China (e-mail: eekhaled@ust.hk).

surface (RHS) [1] [14], which is able to realize hybrid cooperative beamforming (HCBF) at the transceiver using only a few RF chains [15]. In HCBF, the “cooperation” refers to the joint optimization of digital beamforming (DBF) and holographic beamforming (HoBF), coordinated interference management among multiple users, and joint signal processing between the base station (BS) and the RHS, with the aim of achieving higher signal gain and enhanced interference suppression. As shown in Fig. 1, compared with conventional phased-array beamforming architectures, RHS-based HCBF significantly reduces transceiver hardware cost and power consumption by replacing the large number of power-intensive RF chains, phase shifters, and parallel per-element feeding links with a small number of feeds and amplitude control over a series-fed holographic surface [15]. Notably, although RHS-based HCBF employs fewer RF chains and lower circuit power, this does not imply degraded transmit capability compared with phased arrays of identical sizes, since the much smaller inter-element spacing of RHS allows densely packed sub-wavelength holographic elements to still provide a large effective aperture and directional beamforming gain [15]. Additionally, the material and manufacturing costs of RHS panels are considerably lower than those of the traditional phased antenna array, resulting in a lower hardware cost of RHS. Owing to these compelling advantages, RHS has been widely regarded as a promising next-generation reconfigurable antenna (NGRA) technology.

Therefore, the integration of RHS-assisted HCBF into mmWave IoV systems is expected to provide a promising and practical paradigm for supporting the rapidly growing demands of IoV communications in dynamic and complex environments.

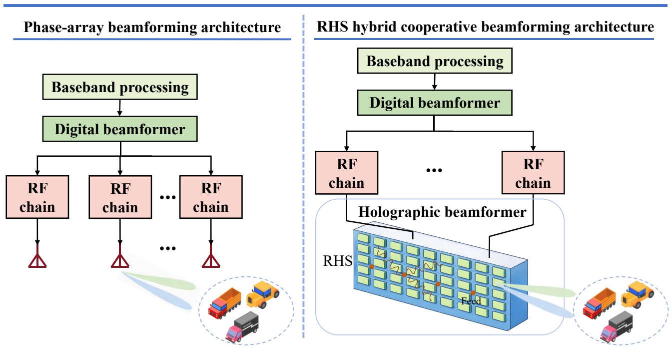

	Phase-array antenna	RHS
Implement	Large number of RF chains	Reduced number of RF chains, RHS
Element spacing	Half-wavelength spacing	One quarter wavelength
Power consumption	High	Low
Material and manufacturing costs	High	Low

Fig. 1: Structural comparison between phased array and RHS beamforming architectures.

B. Related Work

1) Application of RHS in wireless communications: Since the concept of RHS was first introduced in [14], its feasibility for dynamic multi-beam steering in wireless communication networks, thereby enhancing transmission performance, has been demonstrated from both physical and algorithmic perspectives [16]–[18]. Specifically, in [16], an RHS design capable of generating multi-beam radiation patterns was proposed, where each element’s amplitude was allowed to be controlled via the ON/OFF state of its built-in PIN diode. Similarly, in [17], another type of RHS utilizing liquid crystal materials for the radiation elements was proposed, where the amplitude of each element was adjusted by tuning the liquid crystal capacitance. Additionally, in [18], an effective sidelobe cancellation algorithm was designed to optimize the beam pattern of RHSs.

2) HCBF Optimization in RHS-assisted wireless communications: More recently, the HCBF optimization exploiting RHS has also been extensively studied in various wireless network scenarios [19]–[26], including traditional multi-user networks [19], [20], low Earth orbit (LEO) satellite communication networks [21], edge computing networks [22], positioning systems [23], radar and radar-communication systems [24]–[26]. Particularly, in [19] and [20], the sum rate and hardware impairment-constrained energy efficiency (EE) were maximized, respectively, by optimizing HCBF in RHS-assisted multi-user networks. In [21], the sum rate was maximized by optimizing HCBF in RHS-assisted LEO satellite communication networks. Besides, in [22], the latency in RHS-assisted distributed edge computing networks was minimized by jointly optimizing the portion of tasks processed locally, the local computing frequency, and the HCBF. Also, in [23], the positioning error was minimized for multi-band RHS-assisted positioning systems by jointly optimizing the HCBF, the position estimator vector, sets of adaptation functions, and the scheduling probability vectors. Furthermore, in [24] and [25], multi-target detection accuracy was maximized for the RHS-assisted radar systems by jointly optimizing the radar waveform and RHS amplitudes. Moreover, in [26], radar signal-to-interference-plus-noise ratio (SINR) was maximized for the RHS-assisted wideband dual-function radar-communication systems with frequency-selective reconfigurable intelligent surface, by jointly optimizing the HCBF and passive beamforming.

3) Learning-based Optimization of IoVs: Nevertheless, existing works have primarily optimized HCBF in non-IoV systems via conventional convex theory-based iterative methods, and have yet to study RHS-based HCBF in mmWave IoV systems. Compared to other wireless networks, IoV networks exhibit significantly higher dynamics due to the mobility of MVs, which leads to time-varying channels, as well as frequent access and departure of MVs, resulting in frequent changes in network topology [27]. Under such conditions, if conventional iterative optimization methods are deployed, they require frequent recalculation to update the beamforming vectors and resource allocation, which gives rise to high computational complexity and low efficiency. To better accom-

---

[1] The RHS considered in this paper is totally different from the reconfigurable intelligent surface (RIS) [12], [13]. Specifically, the RIS is generally used as a passive relay in wireless communications, while the RHS is integrated with the transceiver serving as a metamaterial antenna.

modate practical dynamic environments, some recent works have proposed machine learning (ML)-based methods, such as deep reinforcement learning (DRL)-based [28], [29] and graph neural networks (GNN)-based [30]–[34] methods, which are capable of handling the high dynamics of IoV by adapting to rapidly changing environments. Specifically, in [28], energy consumption, latency, and cost were jointly optimized within a multi-objective framework, where a double deep Q-network was employed to perform real-time perception and feature extraction of system states in IoVs. In [29], three DRL-based methods were designed to independently optimize task offloading decisions and computation resource allocation for the IoVs. Furthermore, heterogeneous-GNN-based methods [30], [31] and dynamic-GNN-based methods [32], [33] were proposed to optimize service mode selection and target vehicle association in IoV integrated sensing and communication systems. An integrated GNN and multi-agent DRL method [34] was proposed to optimize distributed resource allocation in dynamic IoVs.

C. Motivation and Contributions

Although DRL-based methods can learn online decision policies for dynamic IoV environments, they rely on fixed-dimensional neural network (NN) architectures. Therefore, when the number of connected MVs changes, the NN structure often needs to be redefined and the model retrained, resulting in high computational overhead. In contrast, GNN-based methods can naturally accommodate variable-size IoV topologies through graph representations and parameter sharing. However, despite their structural adaptability, GNN-based methods do not guarantee the preservation of previously learned topology-dependent beamforming knowledge when updated on newly encountered scenarios. Thus, direct fine-tuning may cause catastrophic forgetting, whereas retraining from scratch for each new scenario remains inefficient. To address these challenges, we employ the lifelong graph learning (LGL) framework for efficient HCBF optimization in RHS-assisted mmWave IoV systems, since it naturally supports incremental learning across tasks by transferring previously acquired knowledge to new learning tasks while preserving important knowledge learned from earlier ones.

To the best of our knowledge, this is the first work on designing an LGL-based method for addressing dynamic optimization challenges in IoVs, as LGL was originally presented in the field of graph learning [35] to tackle the problem of lifelong learning over dynamically evolving graph-structured data, such as social networks [36], traffic prediction [37], and recommender systems [38]. Designing an LGL-based HCBF optimization method (LGL-HCBF) for IoVs is non-trivial, as it requires balancing plasticity and stability. Specifically, in IoVs, the dynamic evolution of network topology requires LGL-HCBF to possess sufficient plasticity so that it can continually learn new topology features and rapidly adapt to newly encountered scenarios. Meanwhile, given that similar network conditions may repeatedly arise in practical IoVs, the LGL-HCBF should possess sufficient stability to effectively retain and accumulate knowledge learned from previous scenarios. As a result, striking an effective balance between enhancing the model's adaptability to new scenarios and preventing the forgetting of historical knowledge remains a significant and challenging problem in IoVs. To address this challenge, we propose two mechanisms, i.e., a knowledge replay mechanism and a weight consolidation mechanism. The main contributions of this paper are summarized as follows.

- To enable green mmWave IoV communications, an RHS-based HCBF scheme is proposed by leveraging the low-cost and low-power characteristics of the RHS. As it is difficult to acquire perfect CSI in practical IoV scenarios, we formulate a transmit power minimization problem taking into account imperfect CSI by optimizing the HCBF matrix for each scenario, subject to satisfying the rate requirements of each MV.
- Due to the non-convexity of the formulated optimization problem, as well as dynamic network topology variations and time-varying channel conditions, an LGL-HCBF optimization method is proposed, in which an incremental graph convolutional network (IGCN)-based beamformer is developed to facilitate parameter sharing and exchange of local structural information across different graph structures, thereby providing stronger adaptability to rapid changes in IoV scenarios.
- To address the stability-plasticity dilemma of LGL-HCBF, we propose two complementary mechanisms, i.e., knowledge replay mechanism and weight consolidation mechanism, which work collaboratively to preserve important knowledge learned from previous scenarios during incremental updates. A stability–plasticity tradeoff factor is introduced to balance stability and plasticity.
- Simulation results show that the proposed RHS-based HCBF scheme achieves lower power consumption than traditional phased-array beamforming schemes under identical hardware cost, deployment scales, and rate constraints. Moreover, the proposed LGL-HCBF exhibits superior adaptability by leveraging knowledge learned from similar scenarios, and achieves a higher approximation ratio on previously learned scenarios, consistently outperforming other baseline LGL methods in terms of stability and transferability.

The remainder of the paper is structured as follows. Section II introduces the system model of the RHS-assisted IoV networks and formulates the transmit power minimization problem. Section III presents the proposed LGL-HCBF method, and provides a detailed explanation of the algorithmic process. Section IV provides extensive simulation results associated with the RHS and the proposed method, while the conclusions of the work are summarized in Section V.

Notation: In this paper, lower-case letters represent scalars, lower-case bold letters denote column vectors, and upper-case bold letters indicate matrices. The superscripts $(\cdot)^T$ and $(\cdot)^H$ refer to the transpose and conjugate transpose operators, respectively. $\mathbb{C}^{M\times N}$ and $\mathbb{R}^{M\times N}$ denote $M \times N$ complex and real matrix spaces, respectively. The Euclidean norm of a vector $\mathbf{a}$ is denoted by $\|\mathbf{a}\|_2$, and its squared norm is denoted by $|\mathbf{a}|^2$. The notation $\mathrm{Diag}(\mathbf{a})$ forms a diagonal matrix from

TABLE I
List of Notations

Symbol	Definition
M	Number of RHS elements.
N	Number of feeds (RF chains) of the RHS.
$\mathcal{M}_y,\ \mathcal{M}_z$	Index sets of RHS elements along y and z axes.
$M_y,\ M_z$	Number of RHS elements along y- and z-axis.
$s \in \mathcal{S}$	Scenario (topology) index; $\mathcal{S}$: set of scenarios.
l	MV index in scenario s.
t	Time-slot index; T: sampling period.
$\mathbf{h}_l^s[t]$	BS-MV channel vector for MV l in scenario s at time slot t.
L_l^s	Number of propagation paths of the BS-MV link.
$\beta_{l,i}^{s,t}$	Complex gain of the i-th path at time slot t.
$h_{l,i}^{s,t}$	Large-scale fading coefficient of the i-th path at time slot t.
$\mathrm{PL}(\cdot)$	Path loss (dB); α: path-loss exponent; D: link distance.
PL_0	Path loss at the reference distance of 1 meter.
PL_s	Shadow fading; σ_s^2: its variance.
$\mathbf{a}(\phi, \psi)$	Transmit steering vector.
$\phi_{l,i}^s,\ \psi_{l,i}^s$	Azimuth/elevation AoD of the i-th path for MV l in scenario s.
$d_y,\ d_z$	RHS element spacing along y and z axes.
λ	Carrier wavelength.
ρ_l^s	Temporal correlation coefficient.
$f_l^{\ s}$	Maximum Doppler shift for MV l in scenario s.
$\hat{\mathbf{h}}_l^s[t-T]$	Estimated CSI at the beginning of the previous slot.
$\Delta\mathbf{h}_l^s[t]$	Channel error term.
$\mathbf{\Sigma}_l^s$	Error covariance matrix.
$\mathbf{V}_s$	DBF matrix in scenario s.
$\mathbf{v}_{s,l}$	Digital beamforming vector for MV l in scenario s.
$\mathbf{\Psi}$	Reference wave matrix.
$\boldsymbol{M}_s$	Holographic amplitude matrix in scenario s.
u_{m_y,m_z}^s	Amplitude of RHS element (m_y, m_z) in scenario s.
$\mathbf{Q}_s$	HoBF matrix in scenario s.
$R_l^s[t]$	Achievable rate of MV l in scenario s at time slot t.
$\tilde{R}_l^s$	Minimum rate requirement of MV l in scenario s.
σ^2	Noise power.
P_s	Total transmit power at the BS in scenario s.
$P_s^{\max}$	Maximum transmit power constraint at the BS in scenario s.
$\mathcal{T}$	Sequence of learning tasks.
$\boldsymbol{e}_{z_s}^s$	Exemplar in training stage s.
Δ_{s,z_s}	Performance evaluation metric for exemplar $\boldsymbol{e}_{z_s}^s$ at stage s.
Δ_{s,z_s}^*	Stored soft label of exemplar $\boldsymbol{e}_{z_s}^s$ obtained at training stage s.
$\zeta,\ \delta_s$	Balance factors in $\Delta(\cdot)$.
P_{s,z_s}	BS transmit power for exemplar $\boldsymbol{e}_{z_s}^s$ at training stage s.
$R_{z_s,i}^s$	Achievable rate of the i-th MV in exemplar $\boldsymbol{e}_{z_s}^s$ at stage s.
$\tilde{R}_{z_s,i}^s$	Rate requirement of the i-th MV in exemplar $\boldsymbol{e}_{z_s}^s$ at training stage s.
ξ	Stability-plasticity tradeoff factor.

vector $\mathbf{a}$, and $\mathrm{diag}(\mathbf{A})$ extracts the diagonal vector from matrix $\mathbf{A}$. The calligraphic uppercase letter $\mathcal{A}$ denotes a set. The expectation operator is denoted by $\mathbb{E}\{\cdot\}$, and $\otimes$ represents the Kronecker-product operation. The circularly symmetric complex Gaussian (CSCG) distribution with mean zero and variance $\mathbf{\Sigma}$ is represented as $\mathcal{CN}(0, \mathbf{\Sigma})$.

II. System Model and Problem Formulation

A. Network Model

As illustrated in Fig. 2, we consider a typical downlink multiple-input single-output (MISO) mmWave IoV communication system. Specifically, the BS transmits multiple data streams to multiple single-antenna MVs. To reduce overall system hardware cost and power consumption, an RHS panel is integrated at the BS to perform HCBF by leveraging the holographic principle, thereby reducing the need for large-scale RF chains and phase-shifting circuits [39]. Generally, the RHS consists of three main components, i.e., M sub-wavelength RHS elements, N feeds, and a waveguide. The RHS elements are arranged in a uniform planar array (UPA) on the y-z plane, forming an array size of $M = M_{\mathrm{y}} \times M_{\mathrm{z}}$, where M_{y} and M_{z} represent the number of elements along the y and z axes, respectively. These elements are indexed by the sets $\mathcal{M}_{\mathrm{y}} = \{1, \ldots, m_{\mathrm{y}}, \ldots, M_{\mathrm{y}}\}$ and $\mathcal{M}_{\mathrm{z}} = \{1, \ldots, m_{\mathrm{z}}, \ldots, M_{\mathrm{z}}\}$. In contrast to conventional phased-array architectures, which rely on per-element phase shifters and parallel feeding networks, the RHS adopts a fundamentally different operating mechanism based on reference-wave propagation and amplitude-controlled elements. Due to the dynamic mobility of MVs, they frequently enter or exit the network coverage area, leading to dynamic changes in the IoV network topology.

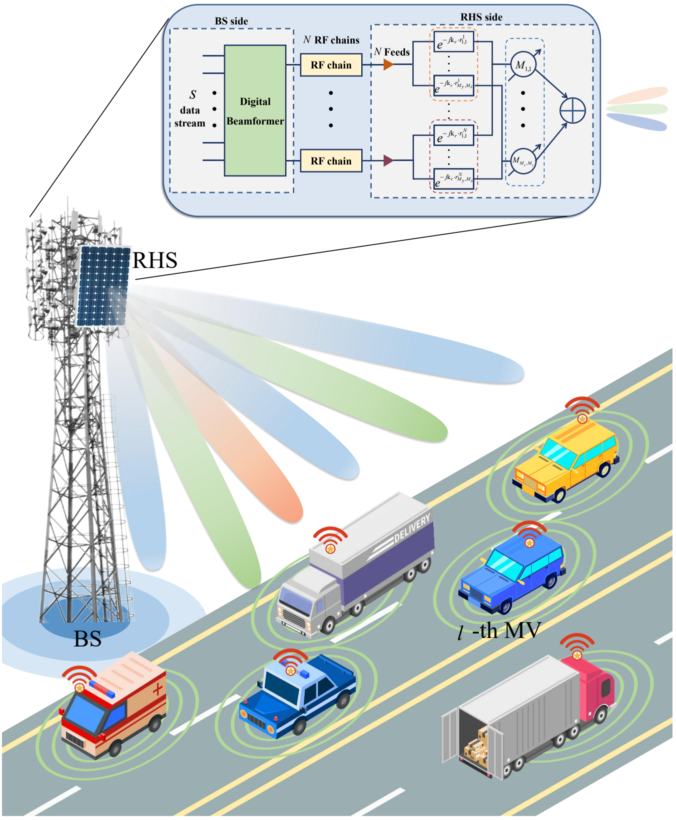

Fig. 2: System model of RHS-assisted mmWave IoV.

Definition 1: ***(The s-th Scenario)*** The network topology consisting of s connected MVs simultaneously served by the BS is defined as the s-th scenario.

According to *Definition 1*, for an IoV system with S MVs, there exist at most S possible network scenarios [2], forming the scenario set denoted as $\mathcal{S} = \{1, \ldots, s, \ldots, S\}$. Particularly, in the s-th scenario, the l-th MV is denoted with l for short, where $l \in \{1, ..., s\}$.

---

[2] It is worth clarifying that the scenario index does not correspond to independent mobility patterns. Instead, all scenarios are extracted from a continuous mobility process by grouping time slots according to the number of connected MVs.

B. Channel Model

1) MmWave Channel Model: According to [40]–[43], a time-varying Saleh-Valenzuela scattering model is considered to characterize the mmWave channels when the Doppler effect is introduced. Specifically, let $\mathbf{h}_l^s[t] \in \mathbb{C}^{M\times 1}$ denote the channel gain from the BS to the l-th MV in the s-th scenario at time slot t, given by

$$\mathbf{h}_l^s[t] = \sqrt{\frac{M}{L_l^s}} \sum_{i=1}^{L_l^s} \beta_{l,i}^{s,t} \mathbf{a}\left(\phi_{l,i}^s, \psi_{l,i}^s\right), \tag{1}$$

where $\sqrt{\frac{M}{L_l^s}}$ is a normalization factor, L_l^s represents the number of propagation paths for the BS-MV links, with $i = 1$ denoting the line-of-sight (LoS) path, $i \geq 2$ denoting the non-LoS (NLoS) paths. $\beta_{l,i}^{s,t} = h_{l,i}^{s,t} e^{j2\pi f_l^{s,i} tT}$ denotes the time-varying complex gains incorporating the Doppler shift $f_l^{s,i}$ and sampling period T, respectively. The large-scale fading coefficient of the i-th propagation path for the l-th MV at time slot t is defined as $h_{l,i}^{s,t} \sim \mathcal{CN}\left(0, 10^{-0.1\mathrm{PL}_{l,i}^{s,t}}\right)$, where $\mathrm{PL(dB)} = \mathrm{PL}_0 + 10\alpha \log_{10}(D) + \mathrm{PL}_s$, PL_0 is the path loss at the reference distance of one meter, α denotes the path-loss exponent, D (in meters) represents the individual link distance, and $\mathrm{PL}_s \sim \mathcal{CN}\left(0, \sigma_s^2\right)$ is the shadow fading with variance σ_s^2. Similar to [44], $\mathbf{a}\left(\phi_{l,i}^s, \psi_{l,i}^s\right) \in \mathbb{C}^{M\times 1}$ denotes the transmit steering vector for the l-th MV corresponding to the i-th propagation path, which is given by

$$\mathbf{a}\left(\phi_{l,i}^s, \psi_{l,i}^s\right) = \mathbf{a}_{\mathrm{y}}\left(\phi_{l,i}^s, \psi_{l,i}^s\right) \otimes \mathbf{a}_{\mathrm{z}}\left(\psi_{l,i}^s\right), \quad \forall s, l, i, \tag{2}$$

where $\phi_{l,i}^s$ and $\psi_{l,i}^s$ are the i-th angles of departure (AoD) in azimuth and elevation of the l-th MV in the s-th scenario, respectively. Specifically, $\mathbf{a}_{\mathrm{y}}\left(\phi_{l,i}^s, \psi_{l,i}^s\right)$ denotes the y-axis steering vector of the i-th path for the l-th MV in the s-th scenario, which is given by

$$\begin{aligned}\mathbf{a}_{\mathrm{y}}\left(\phi_{l,i}^s, \psi_{l,i}^s\right) = &\frac{1}{\sqrt{M_{\mathrm{y}}}}\left[1, e^{j\frac{2\pi}{\lambda} d_y \sin\phi_{l,i}^s \sin\psi_{l,i}^s}, \dots,\right. \\ &\left. e^{j(M_{\mathrm{y}}-1)\frac{2\pi}{\lambda} d_y \sin\phi_{l,i}^s \sin\psi_{l,i}^s}\right]^T, \quad \forall s, l, i,\end{aligned} \tag{3}$$

and $\mathbf{a}_{\mathrm{z}}\left(\psi_{l,i}^s\right)$ denotes the steering vector along the z-axis of the i-th path for the l-th MV in the s-th scenario, which is

$$\begin{aligned}\mathbf{a}_{\mathrm{z}}\left(\psi_{l,i}^s\right) = &\frac{1}{\sqrt{M_{\mathrm{z}}}}\left[1, e^{j\frac{2\pi}{\lambda} d_z \cos\psi_{l,i}^s}, \dots,\right. \\ &\left. e^{j(M_{\mathrm{z}}-1)\frac{2\pi}{\lambda} d_z \cos\psi_{l,i}^s}\right]^T, \quad \forall s, l, i,\end{aligned} \tag{4}$$

with d_y and d_z being the element spacing of the RHS along the y- and z-axes, respectively, and λ being the carrier wavelength.

2) Imperfect CSI: Due to the high mobility of MVs and the resulting short coherence time in IoV systems, channel estimates quickly become outdated, making it impractical for the BS to acquire perfect CSI [45]–[47]. In this context, the temporal correlation coefficient, denoted as ρ_l^s, is introduced to characterize the correlation between the true CSI and the outdated CSI, based on the Jakes' model [48], [49]. Specifically, $\rho_l^s = J_0\left(2\pi f_l^s T\right)$, where J_0 is the zeroth-order Bessel function of the first kind, and $f_l^s = \max\left(f_l^{s,1}, \dots, f_l^{s,L_l^s}\right)$ represents the maximum Doppler shift. Therefore, the channel evolution over time can be modeled as a function of the value estimated at the beginning of the time slot, plus an unknown residual error that obeys a certain distribution [50], which is given by

$$\mathbf{h}_l^s[t] = \rho_l^s \hat{\mathbf{h}}_l^s[t-T] + \Delta\mathbf{h}_l^s[t], \quad \forall t, \tag{5}$$

where $\hat{\mathbf{h}}_l^s[t-T]$ denotes the estimated outdated CSI, $\Delta\mathbf{h}_l^s[t]$ represents the unknown residual error that follows $\Delta\mathbf{h}_l^s[t] \sim \mathcal{CN}\left(\mathbf{0}, \left(1 - \left|\rho_l^s\right|^2\right)\boldsymbol{\Sigma}_l^s\right)$, and $\boldsymbol{\Sigma}_l^s \succeq \mathbf{0}$ is the positive semidefinite error covariance matrix.

C. RHS-based HCBF Transmission Model

Since the RHS panel lacks digital processing capability, baseband signal processing is performed at the BS. As shown in Fig. 2, for the s-th scenario, the intended signal vector for MVs is denoted as $\boldsymbol{x}_s[t] = \left[x_1^s[t], \dots, x_s^s[t]\right]^T \in \mathbb{C}^{s\times 1}$, and the BS encodes s data streams via a DBF matrix $\boldsymbol{V}_s = \left[\boldsymbol{v}_1^s, \dots, \boldsymbol{v}_s^s\right] \in \mathbb{C}^{N\times s}$. The processed signals are then up-converted to the carrier frequency by the RF chains, each of which feeds to the corresponding RHS feed. These feeds transform the high-frequency currents into electromagnetic waves, represented by the reference-wave matrix $\boldsymbol{\Psi} \in \mathbb{C}^{M\times N}$. Accordingly, the reference wave generated by feed n at the $(m_{\mathrm{y}}, m_{\mathrm{z}})$-th radiation element is given by

$$\Psi_{m_{\mathrm{y}},m_{\mathrm{z}}}^n = e^{\left(-j\mathrm{k}_r\cdot r_{m_{\mathrm{y}},m_{\mathrm{z}}}^n\right)}, \tag{6}$$

where k_r is the propagation vector of the reference wave, and $r_{m_{\mathrm{y}},m_{\mathrm{z}}}^n$ is the distance vector from the feed n to the $(m_{\mathrm{y}}, m_{\mathrm{z}})$-th element. The reference wave propagates along the RHS through the waveguide, exciting the RHS elements. The amplitude of the reference wave at each element is controlled by the holographic amplitude matrix $\boldsymbol{M}_s \in \mathbb{R}^{M\times M}$, which is

$$\boldsymbol{M}_s = \mathrm{Diag}\left(u_{1,1}^s, u_{1,2}^s, \dots, u_{M_{\mathrm{y}},M_{\mathrm{z}}}^s\right), \tag{7}$$

with $u_{m_{\mathrm{y}},m_{\mathrm{z}}}^s \in [0, 1]$ denoting the continuous amplitude-control coefficient of the RHS elements for modulating the reference wave. In an ideal case, the radiation elements whose radiated waves are in phase with the desired directional beam are tuned to radiate strongly, while the radiation elements that are out of phase are detuned so as not to radiate. Therefore, the HoBF matrix $\boldsymbol{Q}_s \in \mathbb{C}^{M\times N}$ for the s-th scenario is given by

$$\boldsymbol{Q}_s = \boldsymbol{M}_s \boldsymbol{\Psi}. \tag{8}$$

The desired directional beams are generated by the coherent superposition of electromagnetic waves from the activated RHS elements. Since the feeds of the RHS are directly connected to the RF chains, no channel attenuation occurs between BS and RHS. As a result, the signal received by the l-th MV in the s-th scenario at time slot t is given by

$$y_l^s[t] = \mathbf{h}_l^s[t]^H \boldsymbol{Q}_s \boldsymbol{v}_l^s x_l^s[t] + \mathbf{h}_l^s[t]^H \boldsymbol{Q}_s \sum_{l'\neq l} \boldsymbol{v}_{l'}^s x_{l'}^s[t] + z_l^s[t], \tag{9}$$

where $\boldsymbol{v}_l^s \in \mathbb{C}^{N\times 1}$ is the l-th column of the matrix $\boldsymbol{V}_s$, and $z_l^s[t] \sim \mathcal{CN}\left(0,\sigma^2\right)$ is the additive white Gaussian noise. Thus, the achievable rate of the l-th MV in the s-th scenario is

$$R_l^s[t] = \log_2\left(1+\frac{\left|\mathbf{h}_l^s[t]^H \boldsymbol{Q}_s \boldsymbol{v}_l^s\right|^2}{\sigma^2+\sum_{l'\neq l}\left|\mathbf{h}_l^s[t]^H \boldsymbol{Q}_s \boldsymbol{v}_{l'}^s\right|^2}\right). \tag{10}$$

Finally, the total transmit power at the BS in the s-th scenario is given by

$$P_s = \mathrm{Tr}\left(\boldsymbol{Q}_s \boldsymbol{V}_s \boldsymbol{V}_s^H \boldsymbol{Q}_s^H\right). \tag{11}$$

D. Problem Formulation

We aim to minimize the total transmit power at the BS across various topology scenarios $\mathcal{S}$ with different numbers of MVs, by jointly designing the DBF matrix $\boldsymbol{V}_s$, and the HoBF matrix $\boldsymbol{Q}_s$ for each scenario $s \in \mathcal{S}$, while satisfying the MV rate requirements, the BS maximum transmit power constraint, and the RHS amplitude constraint under imperfect CSI. Accordingly, the optimization problem for the s-th scenario is formulated as

$$\min_{\boldsymbol{V}_s,\boldsymbol{Q}_s} \; P_s \tag{12a}$$

$$\text{s.t. } R_l^s \geq \tilde{R}_l^s, \quad \forall l \in \{1,\ldots,s\}, \forall s \in \mathcal{S}, \tag{12b}$$

$$P_s \leq P_{\max}^s, \quad \forall s \in \mathcal{S}, \tag{12c}$$

$$u_{m_y,m_z}^s \in [0,1], \quad \forall m_y \in \mathcal{M}_y, \forall m_z \in \mathcal{M}_z, \tag{12d}$$

where $\tilde{R}_l^s$ is the minimum required rate threshold for the l-th MV and $P_{\max}^s$ is the maximum transmit power of the BS in the s-th scenario. Specifically, constraint (12b) indicates that the achievable rate for the l-th MV should meet its required threshold, ensuring that each MV satisfies its minimum rate requirement across different scenarios. Constraint (12c) imposes a maximum transmit power at the BS. Constraint (12d) defines the allowable range of amplitudes for the RHS elements. Considering imperfect CSI, the RHS-assisted IoV system should be capable of achieving robust HCBF optimization, satisfying certain communication rates while minimizing power consumption.

The optimization problem (12) involves multiple scenarios, each with distinct network topologies, which introduces additional complexity, as the model must generalize across these scenarios. Besides, it is noted that the problem in (12) is NP-hard because of the non-convex constraints and the highly coupled variables, which involve optimization in the complex domain with multiplicative coupling of the variables, while being subject to amplitude constraints defined in the real domain for each scenario. On this basis, both conventional mathematical optimization methods and learning-based approaches such as DRL [51] are not well suited to the formulated problem, since the former typically require multiple iterative optimization under channel variations, whereas the latter often need to be retrained from scratch when the topology changes, both of which incur substantial computational overhead and limit rapid adaptation. The above challenges have motivated the development of the LGL method in recent years, which is capable of continuously learning rather than training from scratch when the topology changes, while maintaining the performance in previously learned scenarios. Instead of explicitly solving the NP-hard problem through online iterative optimization, the LGL method reformulates the original problem as a graph learning task and trains a GNN-based beamformer to learn the mapping from topology-dependent imperfect CSI to the corresponding DBF and HoBF solution. In this way, the difficulty caused by the non-convex and coupled variables is shifted from repeated online optimization to offline model training. During deployment, only graph construction and one forward inference are required to generate the beamforming solution. Therefore, the LGL-HCBF method is proposed to address such problems in the following section.

III. PROPOSED LGL-HCBF METHOD

A. Theory Background

The LGL method is a paradigm dedicated to enabling GNNs to effectively handle continuously evolving graph structures and data throughout long-term learning [52]. It combines the concepts of GNN [53] and lifelong learning [54]–[56], aiming to leverage knowledge from previous learning tasks to assist the model in continuously learning to solve new tasks while preserving the knowledge learned from previous ones [35]. In LGL, learning tasks are presented to the GNN model sequentially, where each learning task is trained by fine-tuning the GNN model based on the previous learning task. However, naive fine-tuning can lead to catastrophic forgetting, where the model forgets the old knowledge from previous learning tasks when trained on new learning tasks [52]. In the worst case, newly acquired knowledge may completely overwrite old knowledge, making it inaccessible. Conversely, being overly cautious about updating its parameters to avoid forgetting past knowledge would prevent rapid adaptation to new learning tasks. This phenomenon is called the stability-plasticity dilemma [57]. Therefore, the LGL method should be designed properly not only to maintain plasticity for integrating new knowledge, but also to keep stability to retain previous knowledge.

B. Architecture of the Proposed LGL-HCBF Method

To minimize the BS transmit power by jointly optimizing the DBF and HoBF under imperfect CSI, the proposed method first models the downlink transmission scenario of the IoV as a fully connected directed (FCD) graph. The graph structure directly affects the joint DBF-HoBF optimization by transforming explicit inter-link interference and coupling relationships in the analytical formulation into structured information propagation in the embedding space. Specifically, the achievable rate of each MV depends not only on its own digital and holographic beamforming vectors, but also on the beamforming decisions associated with other MVs due to multi-user interference and shared transmit power constraints. This creates strong cross-link coupling in both the objective function and the constraints. To reflect this structure, each BS–MV communication link is regarded as a node, with node feature embedding imperfect CSI (i.e., $\hat{\mathbf{h}}_l^s$) to characterize the link gain. Each edge represents the interference relationship between MVs, with the normalized inter-vehicle distance and

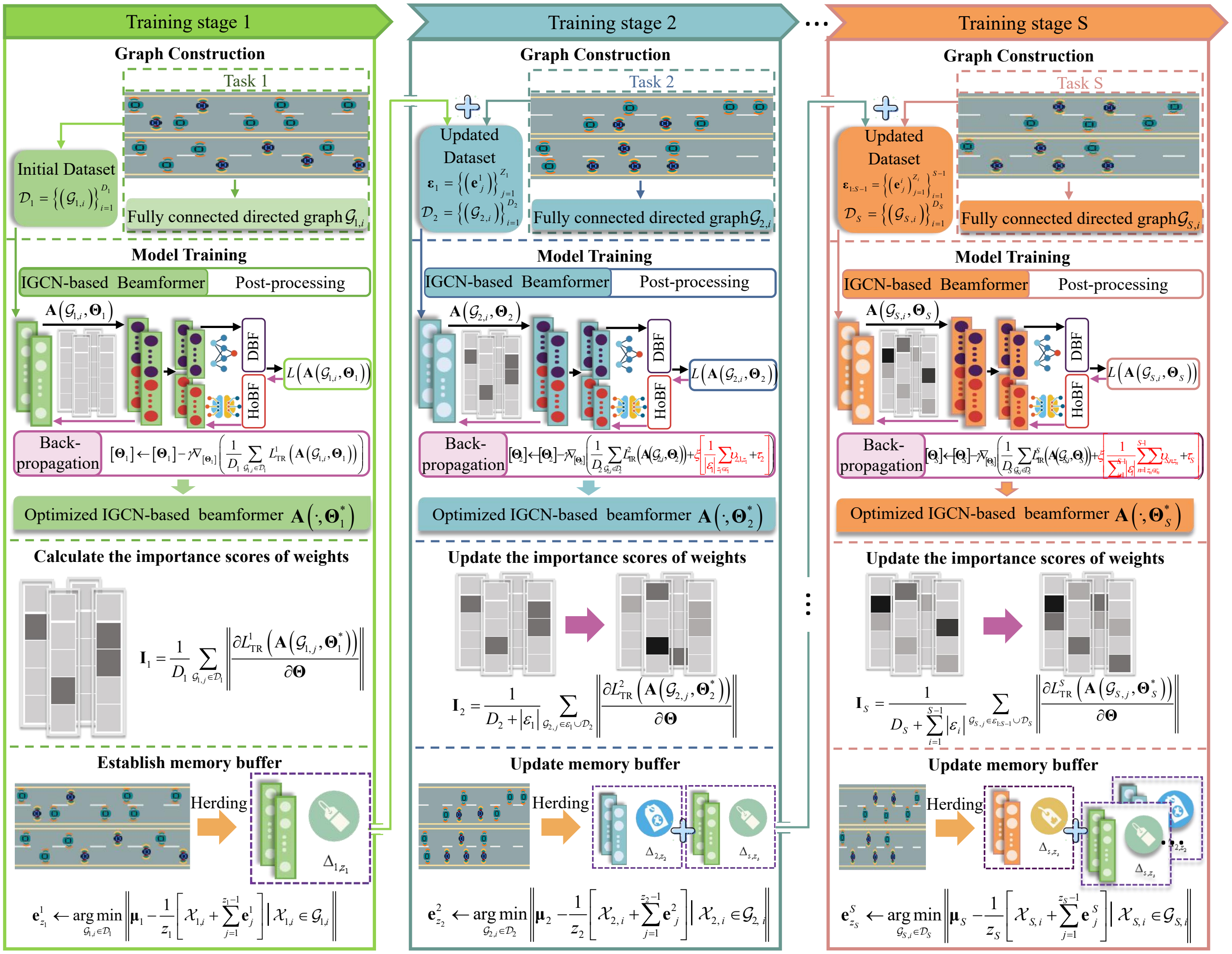

Fig. 3: Architecture of the proposed LGL-HCBF method.

lane index adopted as edge features to encode geometric proximity and spatial configuration, which together determine the interference strength in the physical channel. Whenever MVs enter or exit the coverage area, the graph is adaptively updated by adding or removing the corresponding nodes and associated edges, without redefining the network architecture. The same IGCN parameters are shared across all nodes and edges, and each node aggregates information from its current neighbors through a permutation-invariant operator (e.g., sum). Therefore, the layer structure and parameter dimensions remain unchanged when the number of MVs varies, while the output representation is insensitive to node ordering, thereby ensuring scalability and stability to neighborhood variations. With such a construction, each node updates its embedding by aggregating edge-weighted messages from neighboring nodes, thereby capturing an implicit representation of the aggregated interference impact from other links. Through multiple layers of message passing, the IGCN propagates information beyond one-hop neighbors, allowing the node embeddings to capture the complex dependencies inherent in the joint DBF-HoBF optimization, including cross-link coupling, multi-user interference, the shared transmit power constraint, and the common RHS amplitude design, after which the readout layer directly maps these embeddings to the DBF and HoBF decisions.

As time evolves, continuously moving MVs induce dynamic variations in the number of connected vehicles, thereby giving rise to topology scenarios with different connection scales, which can be mapped to different learning tasks in the proposed LGL-HCBF method to enable incremental knowledge transfer and retention in continuously evolving IoV topologies. Specifically, in the learning process, the proposed LGL-HCBF receives a sequence of tasks $\mathcal{T} = \{\mathcal{T}_1, \ldots, \mathcal{T}_s, \ldots, \mathcal{T}_S\}$, each corresponding to an HCBF optimization task under a particular IoV topology scenario, with the objective of minimizing the BS transmit power. The learning task transition is triggered when the number of connected MVs changes, i.e., when one or more MVs enter or leave the coverage area. Topology variations induced by vehicle mobility, such as changes in inter-vehicle distances and CSI evolution, are treated as intra-task dynamics and are modeled within the same learning task via time-varying node and edge features. These learning tasks are learned by the proposed LGL-HCBF method sequentially. According to *Definition 2*, the learning process consists of S training stages for sequentially completing S learning tasks. For each learning task, parameter inheritance is adopted, where the model is initialized using the optimized parameters learned from the previous learning task, thereby providing a fine-tuned starting point for further adaptation. To address the stability-plasticity dilemma of LGL-HCBF, we propose two complementary mechanisms, i.e., a knowledge replay mechanism and a weight consolidation mechanism, which work collaboratively to preserve previously learned knowledge. As shown in Fig. 3, each training stage contains four steps, namely, graph construction, model training, importance scores of weights calculation and memory buffer establishment. Specifically, the graph construction is identical in all training stages. The model training is mainly aimed at training the IGCN, which learn topology-dependent representations and output the corresponding HCBF solution. The importance scores of weights are calculated by the proposed weight consolidation mechanism, which evaluates the contribution of each weight to the previous learning tasks, reduces the plasticity of important weights to make them less susceptible to being overwritten during new task training, and allows unimportant weights to adjust freely, thereby enabling the model to retain prior knowledge while learning new information. Furthermore, the memory buffer stores the samples selected by the proposed knowledge replay mechanism, which replays a small set of representative exemplars from previous learning tasks during the training of new tasks, helping the model preserve knowledge from previous learning tasks. The specific details are described as follows.

Definition 2: (Training stage s) The training stage s is defined as the s-th learning phase of the proposed LGL-HCBF, during which the model is trained for learning task $\mathcal{T}_s$.

1) Training stage 1: The dataset $\mathcal{D}_1 = \left\{\left(\mathcal{G}_{1,i}\right)\right\}_{i=1}^{D_1}$ for the first scenario is adopted in training stage 1 to train the model $\mathbf{\Theta}_1$, aiming to obtain the IGCN-based beamformer $\boldsymbol{A}\left(\cdot, \mathbf{\Theta}_1^*\right)$ by optimizing $\boldsymbol{A}\left(\cdot, \mathbf{\Theta}\right)$, where D_1 represents the number of dataset samples, and $\mathcal{G}_{1,i}$ represents each sample. $\mathbf{\Theta}_1^*$ is the optimized model parameter at training stage 1, which maps the node features to the desired DBF matrix $\boldsymbol{V}_1$ and HoBF matrix $\boldsymbol{Q}_1$. After model training, the importance scores of weights $\boldsymbol{I}_1$ are calculated. Weights that make a large contribution to previous learning tasks are assigned lower plasticity, whereas less important weights are allowed higher plasticity. Meanwhile, a small subset of $\mathcal{D}_1$, selected as exemplars and denoted by $\varepsilon_1 = \left\{\left(e_i^1\right)\right\}_{i=1}^{Z_1}$, is stored in the memory buffer for replay in later training stages, where Z_1 is the number of exemplars and satisfies $Z_1 \ll D_1$.

2) Training stage $s \in (2, \ldots, S)$: Later, training stages after stage 1 are incremental learning stages. In training stage $s \in (2, \ldots, S)$, model $\mathbf{\Theta}_s$ is initialized with the parameters of $\mathbf{\Theta}_{s-1}$ and updated using dataset $\mathcal{D}_s = \left\{\left(\mathcal{G}_{s,i}\right)\right\}_{i=1}^{D_s}$ along with exemplars $\varepsilon_{1:s-1} = \{\varepsilon_1, \varepsilon_2, \ldots, \varepsilon_{s-1}\}$ to obtain $\boldsymbol{A}\left(\cdot, \mathbf{\Theta}_s^*\right)$. After the model training, the importance scores of weights $\boldsymbol{I}_s$ are updated and a small subset of exemplars ε_s is stored in the memory buffer for replay in future training stages.

C. Steps in Each Training Stage

1) Graph Construction: For training stage s, the considered RHS-assisted IoV system for the s-th scenario is modeled as $\mathcal{G}_s \triangleq \{\mathcal{V}_s, \mathcal{E}_s, \mathcal{X}_s, \mathcal{Y}_s\}$, where $\mathcal{V}_s$ represents the node set of BS-MV communication links, and $\mathcal{E}_s$ represents the edge set of MV-MV interference links with $\iota_s = s \times (s-1)$ edges. $\mathcal{X}_s = \{\boldsymbol{x}_{s,l}\}_{l=1}^{s}$ is the set of nodes' features and $\boldsymbol{x}_{s,l}$ is the feature of the l-th node in training stage s. $\mathcal{Y}_s = \{\boldsymbol{e}_{l,l'}^s\}_{l,l' \in \{1,\ldots,s\}}$ denotes the set of edge feature vectors in training stage s, with $\boldsymbol{e}_{l,l'}^s$ being the feature vector of the edge from the l-th node to the l'-th node.

2) Model Training: After converting the considered RHS-assisted IoV into the FCD graph, model $\mathbf{\Theta}_s$ is optimized for learning task s at training stage s. To efficiently optimize the HCBF, an IGCN-based beamformer $\boldsymbol{A}_s$ with $B+2$ blocks is designed. We aim to learn a shared model $\mathbf{\Theta}$ parameterized by $\mathcal{W} = \left\{\boldsymbol{W}^{(b)}\right\}_{b=0}^{B+1}$ that is able to perform well among all learning tasks $\mathcal{T}$.

As shown in Fig. 4, the IGCN-based beamformer $\boldsymbol{A}_s$ starts by embedding the input node and edge features into higher-dimensional representations, capturing deeper features and patterns through nonlinear transformations. Thus, for embedded block $\mathcal{B}_0$, given the input node feature vector $\hat{\boldsymbol{h}}_l^s$, the embedded node feature vector $\boldsymbol{x}_{s,l}^{(1)} \in \mathbb{R}^{C_{\text{ve}}^{(0)}}$ is

$$\boldsymbol{x}_{s,l}^{(1)} = f_3\left(f_2\left(\mathbf{W}_{\text{ve}}^{(0)} f_1\left(\hat{\boldsymbol{h}}_l^s\right)\right)\right), \tag{13}$$

where $f_1(\cdot) : \mathbb{C}^M \rightarrow \mathbb{R}^{2M}$ is the complex-to-real function, $\mathbf{W}_{\text{ve}}^{(0)} \in \mathbb{R}^{C_{\text{ve}}^{(0)} \times 2M}$ denotes the learnable weight matrix in the embedded block $\mathcal{B}_0$, and $C_{\text{ve}}^{(0)}$ is the corresponding dimension. $f_2(\cdot)$ and $f_3(\cdot)$ denote the batch normalization and a nonlinear operation (e.g., ReLU), respectively. For each graph edge, given the distances and lane information between the l-th and the l'-th nodes, the embedded edge feature vector $\boldsymbol{e}_{l,l'}^s \in \mathbb{R}^{C_{\text{ed}}^{(0)}}$ is transformed as

$$\boldsymbol{e}_{l,l'}^s = f_3\left(\mathbf{W}_{\text{ed}}^{(0)} \mathbf{\Gamma}_{l,l'}^s\right), \tag{14}$$

where $\mathbf{\Gamma}_{l,l'}^s = \left[d_{l,l'}^s, LA_l^s, LA_{l'}^s\right]^T$, $d_{l,l'}^s$ and LA_l^s represent the normalized distance between two nodes and the lane index of the l-th node, respectively. $\mathbf{W}_{\text{ed}}^{(0)} \in \mathbb{R}^{C_{\text{ed}}^{(0)} \times 3}$ is the learnable weight matrix for the edge feature, and $C_{\text{ed}}^{(0)}$ is the corresponding dimension.

To capture inter-node relationships, B update blocks, each corresponding to a GCN layer and a ResNet-inspired layer, are used to obtain the structural information. Specifically, each GCN layer consists of three processes, i.e., the message passing, the message aggregation and the node update.

- *Message Passing:* For each edge $l \rightarrow l'$, the message vector $\boldsymbol{m}_{s,l,l'}^{(b)}$ of the b-th GCN layer is formed by concatenating the source node feature $\boldsymbol{x}_{s,l}^{(b)}$, destination node feature $\boldsymbol{x}_{s,l'}^{(b)}$, and the edge feature $\boldsymbol{e}_{l,l'}^s$, which is

$$\boldsymbol{m}_{s,l,l'}^{(b)} = \left[\boldsymbol{x}_{s,l}^{(b)}, \boldsymbol{x}_{s,l'}^{(b)}, \boldsymbol{e}_{l,l'}^s\right], \text{for } b \in \{1, \ldots, B\}, \tag{15}$$

with $\boldsymbol{m}_{s,l,l'}^{(b)} \in \mathbb{R}^{2C^{(b)} + C_{\text{ed}}^{(0)}}$, and $C^{(b)}$ being the feature dimension of the node in the b-th GCN layer.

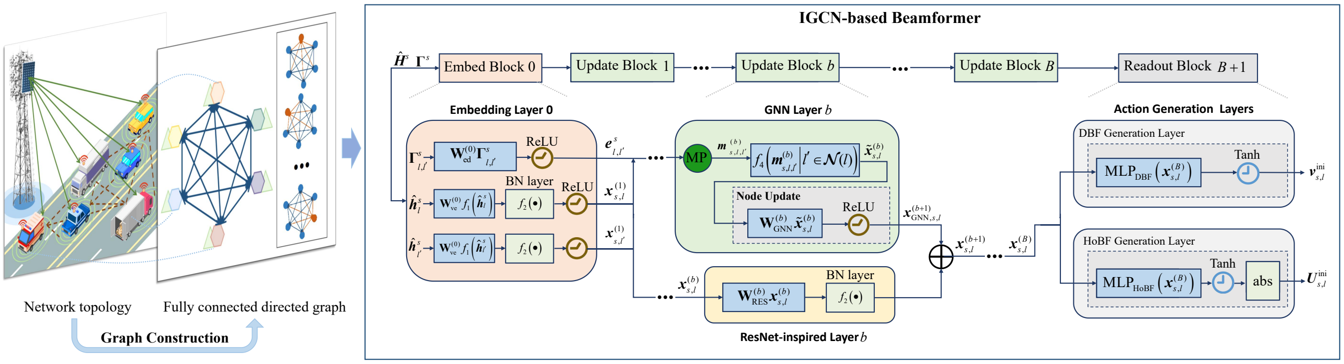

Fig. 4: Structure of IGCN.

- *Message Aggregation:* In the aggregation step, each node aggregates messages from all its neighbors $l' \in \mathcal{N}(l)$, which is expressed by

$$\tilde{x}^{(b)}_{s,l} = f_4\left(m^{(b)}_{s,l,l'} \mid l' \in \mathcal{N}(l)\right), \tag{16}$$

  with $f_4(\cdot) : \mathbb{R}^{\left(2C^{(b)}+C^{(0)}_{\rm ed}\right)\times(s-1)} \to \mathbb{R}^{\left(2C^{(b)}+C^{(0)}_{\rm ed}\right)}$ being the permutation-invariant aggregation function (e.g., sum()).
- *Node Update:* After aggregation, the node feature vector $x^{(b+1)}_{{\rm GCN},s,l} \in \mathbb{R}^{C^{(b+1)}}$ are updated in terms of

$$x^{(b+1)}_{{\rm GCN},s,l} = f_3\left(\mathbf{W}^{(b)}_{\rm GCN}\tilde{x}^{(b)}_{s,l}\right), \tag{17}$$

  where $\mathbf{W}^{(b)}_{\rm GCN} \in \mathbb{R}^{C^{(b+1)}\times\left(2C^{(b)}+C^{(0)}_{\rm ed}\right)}$.

To preserve information flow and mitigate vanishing gradient issues, residual connections are introduced. At each update block, the input node features are also fed into a ResNet-inspired layer, which performs a transformation and then adds the resulting feature vector to the output of the current GCN layer. The combined output is fed into the subsequent update block to generate $x^{(b+1)}_{s,l} \in \mathbb{R}^{C^{(b+1)}}$, ensuring that both the original features and the newly learned representations are jointly exploited in the learning process, as expressed by

$$x^{(b+1)}_{s,l} = f_2\left(\mathbf{W}^{(b)}_{\rm RES}x^{(b)}_{s,l}\right) + x^{(b+1)}_{{\rm GCN},s,l}, \tag{18}$$

where $\mathbf{W}^{(b)}_{\rm RES} \in \mathbb{R}^{C^{(b+1)}\times C^{(b)}}$.

The output $x^{(B)}_{s,l}$ is then fed into the readout block, which consists of a DBF generation layer and a HoBF generation layer to output the initialized DBF vector $v^{\rm ini}_{s,l} \in \mathbb{C}^{2N}$ and the RHS amplitude vector $u^{\rm ini}_{s,l} \in \mathbb{R}^M$, respectively, as given by

$$\begin{cases} v^{\rm ini}_{s,l} = f_5\left(\mathrm{MLP}_{\rm DBF}\left(x^{(B)}_{s,l}\right)\right), \\ u^{\rm ini}_{s,l} = \sqrt{f_5\left(\mathrm{MLP}_{\rm HoBF}\left(x^{(B)}_{s,l}\right)\right)}^2, \end{cases} \tag{19}$$

where $f_5(\cdot)$ represents a nonlinear operation (e.g., Tanh), and MLP denotes multi-layer perceptrons. It is worth noting that the square-and-root operation in Eq. (19) guarantees that the elements of $u^{\rm ini}_{s,l}$ are constrained to the range $[0, 1]$, thereby satisfying the physical and mathematical constraint (12d).

Furthermore, a post-processing step is employed to map the model outputs into optimization variables through a series of mathematical operations. Specifically, the DBF vector is given by $v_{s,l} = P^s_{\max}\overline{v}_{s,l}$, where $\overline{v}_{s,l} = v^{\rm ini}_{s,l,{\rm real}} + j * v^{\rm ini}_{s,l,{\rm imag}}$ is the normalized DBF vector, with $v^{\rm ini}_{s,l,{\rm real}}$ and $v^{\rm ini}_{s,l,{\rm imag}}$ being the real and imaginary outputs of the DBF generation layer, respectively. The holographic amplitude vector is then obtained by averaging the initialized RHS amplitude vectors across all users, i.e.,

$$\bar{u}_s = \frac{1}{s}\sum_{l=1}^{s} u^{\rm ini}_{s,l}, \tag{20}$$

$$M_s = \mathrm{Diag}(\bar{u}_s), \tag{21}$$

where $\bar{u}_s \in \mathbb{R}^M$ denotes the averaged RHS amplitude vector. By taking the arithmetic mean of the initial amplitudes $u^{\rm ini}_{s,i}$ for all MVs in each scenario, the amplitude design of each RHS elements simultaneously accounts for the requirements of all MVs, rather than biasing toward any particular MV.

3) Knowledge Replay Mechanism: In training stage $s \in (2, \ldots, S)$, the knowledge replay mechanism [3] is employed to preserve knowledge acquired in previous training stages and mitigate catastrophic forgetting. Specifically, for each training stage s, a small exemplar set $\varepsilon_s = \left\{e^s_1, e^s_2, \ldots, e^s_{Z_s}\right\}$ is selected for replay, where Z_s is the number of exemplars in the s-th scenario. To improve computational efficiency and reduce storage requirements, the selected exemplars should effectively represent the core characteristics of the dataset. Therefore, the herding method [59] is adopted, which iteratively selects samples closest to the mean of the data distribution, and

$$e^s_{Z_s} \leftarrow \mathop{\arg\min}_{\mathcal{G}_{s,i}\in\mathcal{D}_s}\left\|\mu_s - \frac{1}{Z_s}\left[\mathcal{X}_{s,i} + \sum_{j=1}^{Z_s-1} e^s_j\right]\middle| \mathcal{X}_{s,i} \in \mathcal{G}_{s,i}\right\|, \tag{22}$$

where $\mu_s = \frac{\sum_{\substack{\mathcal{X}_{s,i}\in\mathcal{G}_{s,i} \\ \mathcal{G}_{s,i}\in\mathcal{D}_s}} \mathcal{X}_{s,i}}{D_s}$ is the mean of the data distribution.

Instead of directly using the exemplars to train the model, a *performance-based data regularization* mechanism is introduced to penalize the degradation in performance on exemplars, rather than enforcing exact matching of historical outputs. To this end, a scalar performance evaluation metric $\Delta(\cdot)$

---

[3] This mechanism relies on a retraining process from previous task samples to keep the performance of previous experiences on previously learning tasks [58], [59].

is designed to jointly capture the transmit power consumption and rate-constraint satisfaction for a given exemplar. Specifically, for exemplar $\boldsymbol{e}_{z_s}^s$ at training stage s, the performance evaluation metric is defined as

$$\Delta_{s,z_s} = \zeta \left(P_{s,z_s}\right)^2 + \frac{\delta}{s} \sum_{i=1}^{s} \left(\frac{\tilde{R}_{z_s,i}^s}{R_{z_s,i}^s} - 1 \right)^2, \tag{23}$$

with ζ and δ being the balance factors, P_{s,z_s}, $R_{z_s,i}^s$ and $\tilde{R}_{z_s,i}^s$ denoting the transmit power at the BS for exemplar $\boldsymbol{e}_{z_s}^s$, the achievable rate and the rate requirement of the i-th MV in exemplar $\boldsymbol{e}_{z_s}^s$ in training stage s, respectively. By design, a smaller value of Δ_{s,z_s} indicates better performance, corresponding to lower transmit power and improved constraint satisfaction, whereas a larger value reflects performance degradation or increased constraint violations. For exemplar $\boldsymbol{e}_{z_s}^s$, the corresponding soft label is defined as the performance value attained by the optimized model parameterized by $\boldsymbol{\Theta}_s^*$ at training stages s, which is given by

$$\Delta_{s,z_s}^* = \zeta \left(P_{s,z_s}^*\right)^2 + \frac{\delta}{s} \sum_{i=1}^{s} \left(\frac{\tilde{R}_{z_s,i}^s}{R_{z_s,i}^{s,*}} - 1 \right)^2, \tag{24}$$

where P_{s,z_s}^* and $R_{z_s,i}^{s,*}$ denote the transmit power and achievable rate, respectively. These soft labels serve as performance anchors to characterize the performance achievable by the optimized model on the corresponding exemplars at training stage s. Importantly, these soft labels are stored together with the exemplar in the memory buffer and remain frozen during subsequent training stages. When the model is updated at a later training stage s' $(s' > s)$, its performance on exemplar $\boldsymbol{e}_{z_s}^s$ is evaluated using the same metric, yielding Δ_{s',z_s}. The resulting performance difference is quantified as

$$\upsilon_{s',s,z_s} = \frac{\Delta_{s',z_s} - \Delta_{s,z_s}^*}{1 + e^{-\left(\Delta_{s',z_s} - \Delta_{s,z_s}^*\right)}}. \tag{25}$$

A positive value of υ_{s',s,z_s} indicates that the current model suffers performance degradation on exemplar $\boldsymbol{e}_{z_s}^s$ relative to the stored soft label, whereas a non-positive value indicates that the current model has preserved the previously acquired knowledge on that exemplar, and may even achieve a better solution. With this design, Eq. (25) avoids directly constraining the model to reproduce historical beamforming outputs, and instead regularizes learning at the performance level, thereby preventing error accumulation across training stages, even when the historical solutions are not optimal.

To make the knowledge replay mechanism directly affect model training, the performance differences on all stored exemplars from previous training stages are aggregated into a replay regularization term, which is incorporated into the training stage-s training loss as

$$\mathcal{L}_{\text{KR}}^s(\boldsymbol{\Theta}_s) = \frac{1}{\sum_{i=1}^{s-1} Z_i} \sum_{n=1}^{s-1} \sum_{z_n \in Z_n} \upsilon_{s,n,z_n}. \tag{26}$$

By minimizing this term, the current model is encouraged to preserve the historical performance recorded by the soft labels while adapting to the new learning task, thereby mitigating catastrophic forgetting across training stages.

4) Weight Consolidation Mechanism: After training task $\mathcal{T}_s$, the optimized model parameterized by $\boldsymbol{\Theta}_s^*$ are obtained. It is well known that not all model weights contribute equally. Those weights that significantly contributed to the output are assigned lower plasticity to preserve previously acquired knowledge, while less important weights are given higher plasticity to facilitate adaptation in new learning tasks. Specifically, at training stage s, the importance scores of the model weights are computed based on the gradients of the task-related (TR) loss, where the gradient magnitudes are used as indicators of parameter importance. Accordingly, the importance scores are given by

$$\begin{aligned} \boldsymbol{I}_s = & \frac{1}{D_s + \sum_{i=1}^{s-1} Z_i} \sum_{\mathcal{G}_{s,j} \in (\boldsymbol{\varepsilon}_{1:s-1} \cup \mathcal{D}_s)} \\ & \left\| \frac{\partial L_{\text{TR}}^s \left(\boldsymbol{A} \left(\mathcal{G}_{s,j}, \boldsymbol{\Theta}_s^* \right) \right)}{\partial \boldsymbol{\Theta}} \right\|, \end{aligned} \tag{27}$$

where the TR loss is defined as

$$\mathcal{L}_{\text{TR}}^s = \left(\tilde{P}_s\right)^2 + e^{\frac{\tilde{P}_s}{P_{\max}^s}} + \frac{\alpha \sum_{i=1}^{s} \left(\frac{\tilde{R}_i^s}{R_i^s} - 1 \right)^2}{s}, \tag{28}$$

and α is the balancing hyper-parameter. Accordingly, a weight consolidation term is designed to constrain important parameters from deviating excessively from their previously optimized values, thereby preserving historical knowledge during incremental training, which is given by

$$\mathcal{L}_{\text{WC}}^s(\boldsymbol{\Theta}_s) = \frac{1}{s-1} \sum_{n=1}^{s-1} \boldsymbol{I}_s \otimes \left(\boldsymbol{\Theta}_s - \boldsymbol{\Theta}_n^*\right)^2. \tag{29}$$

The objective of the weight consolidation mechanism is to allow weights with low importance scores to be adjusted more freely, while preserving weights with high importance scores.

In training stage 1, only the task-related objective is considered. For the subsequent training stage $s \in (2, \ldots, S)$, the model should not only minimize the BS transmit power while satisfying the rate requirements of the current scenario, but also preserve the knowledge acquired from previous training stages. To this end, the overall training loss is defined as

$$\mathcal{L}_s(\boldsymbol{\Theta}_s) = \begin{cases} \dfrac{1}{D_s} \displaystyle\sum_{\mathcal{G}_{s,i} \in \mathcal{D}_s} L_{\text{TR}}^s\big(\boldsymbol{A}(\mathcal{G}_{s,i}, \boldsymbol{\Theta}_s)\big), & s = 1, \\ \dfrac{1}{D_s} \displaystyle\sum_{\mathcal{G}_{s,i} \in \mathcal{D}_s} L_{\text{TR}}^s\big(\boldsymbol{A}(\mathcal{G}_{s,i}, \boldsymbol{\Theta}_s)\big) & s \geq 2, \\ \quad + \xi \left[\mathcal{L}_{\text{KR}}^s(\boldsymbol{\Theta}_s) + \mathcal{L}_{\text{WC}}^s(\boldsymbol{\Theta}_s) \right], & \end{cases} \tag{30}$$

where ξ is the stability-plasticity tradeoff factor. Both the knowledge replay mechanism and the weight consolidation mechanism are incorporated into the overall loss as weighted regularization terms, thereby imposing soft constraints rather than hard restrictions on model updating. When the new learning task differs significantly from previous ones, e.g., in the number of MVs, the strength of these regularization terms can be relaxed by adjusting the stability-plasticity tradeoff factor, allowing the current task loss to dominate the parameter optimization and thus preserving sufficient plasticity for adaptation.

Then, the parameters of model $\boldsymbol{\Theta}_s$ are updated according to

$$[\boldsymbol{\Theta}_s] \leftarrow [\boldsymbol{\Theta}_s] - \gamma \nabla_{[\boldsymbol{\Theta}_s]} \mathcal{L}_s(\boldsymbol{\Theta}_s), \tag{31}$$

where γ is the learning rate.

D. Complexity Analysis of LGL-HCBF

The overall computational complexity of the proposed LGL-HCBF method consists of two main components: graph construction and IGCN inference. According to [35], the computational complexity of graph construction is $O\left(2Ms + 3s(s-1)\right)$. The computational complexity of the model inference primarily arises from three components: feature embedding, iterative graph convolutional updates, and readout operations. The computational complexity of the feature embedding is $O(sMC_{ve}^{(0)} + 3s^2C_{ed}^{(0)})$, The core computational load stems from the IGCN, which consists of B update blocks. Each block includes message passing, aggregation, and node update steps with the computational complexity $O\left(s^2 \cdot \left(2C^{(b)} + C_{ed}^{(0)}\right) \cdot C^{(b+1)}\right)$. Lastly, the readout block incur a complexity of $O(sC^{(B)}D)$. Therefore, the overall computational complexity of training is

$$O\Big(sMC_{ve}^{(0)} + s^2C_{ed}^{(0)} + \sum_{b=1}^{B} s^2 \left(2C^{(b)} + C_{ed}^{(0)}\right) C^{(b+1)} + sC^{(B)}D\Big), \tag{32}$$

where the dominant term is $O(Bs^2C^2)$, with C representing the upper bound of the feature dimension per layer. It is worth noting that the two lifelong learning mechanisms are no longer required during inference. The total computational complexity of the proposed method is

$$O\Big(2Ms + 3s(s-1) + sMC_{ve}^{(0)} + s^2C_{ed}^{(0)} + \sum_{b=1}^{B} s^2 \left(2C^{(b)} + C_{ed}^{(0)}\right) C^{(b+1)} + sC^{(B)}D\Big) = O(Bs^2C^2). \tag{33}$$

IV. NUMERICAL RESULTS

In this section, simulation results are provided to demonstrate the advantages of the proposed RHS-based HCBF scheme over traditional phased-array beamforming schemes. Moreover, the proposed LGL-HCBF method is compared with state-of-the-art methods to highlight its superior performance.

A. Simulation Settings

The simulated IoV network consists of a 1 km bidirectional two-lane road segment [60] aligned with the y-axis, where the MVs move along the positive or negative directions of the y-axis. A standard lane width of 3.5 m is adopted to model a typical roadside coverage scenario [60]. Due to vehicle mobility, MVs may continuously enter and leave the coverage area of the BS, which is located at $(0, 10, 20)$, thereby leading to dynamic changes in the network topology. Under this setting, the proposed LGL-HCBF method incrementally learns multiple topology scenarios characterized by different numbers of connected MVs. Specifically, eight representative scenarios are considered, where the number of MVs varies from 2 to 16 to capture traffic conditions ranging from sparse to moderately dense [61]. In particular, the s-th scenario corresponds to a case with s connected MVs, where $s \in \{2, 4, 6, 8, 10, 12, 14, 16\}$, while more congested cases with 18 to 50 connected MVs are also evaluated. Moreover, MV speeds are set within the range of 5–30 m/s to represent mobility levels from urban roads to highways [62], which directly influence the Doppler spread and channel time variations in practical IoV systems. Unless otherwise stated, the system parameters and the hyperparameters of the proposed LGL-based method are summarized in Table II [63].

TABLE II

System Parameters and Hyperparameters Setting.

System parameters	Symbol	Value
Antenna number	N	16
Car velocity	v	5, 10, …, 30 m/s
Maximum transmit power	$P^s_{\max}$	47 dBm
RHS element spacing	d_y / d_z	0.25 cm
Carrier frequency	f	30 GHz
Bandwidth	B_w	600 MHz
Propagation vector on the RHS	k_r	$200\sqrt{3}\pi$
Size of RHS	M	64
Noise density	σ^2	-80 dBm/Hz
Propagation paths number	L^s_l	2
Carrier wavelength	λ	1 cm
Path loss at the reference distance	PL_0	61.4 dB
Path-loss exponent	α	2.2
Variance of shadow fading	σ_s^2	5.8 dB

Hyperparameters	Symbol	Value
Learning rate	γ	4.5×10^{-4}
The number of epochs for each learning task	Λ	5000
The size of dataset for each learning task	D	5000
The size of exemplar for each learning task	ε	50
Batch size	B_s	128
The number of update blocks	B	4

B. Hyperparameters Selection via Simulations

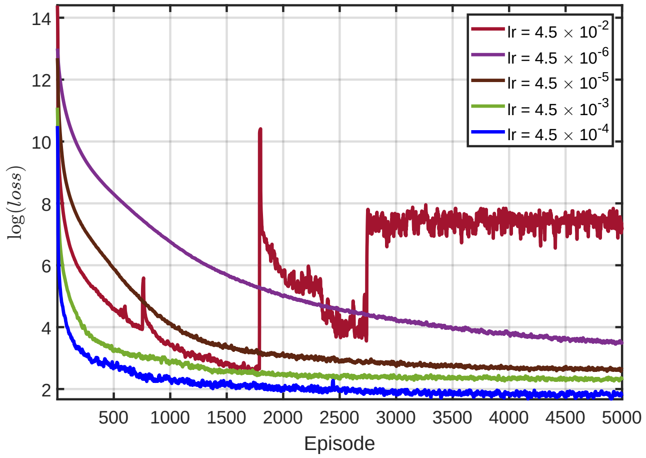

Fig. 5: Convergence rate of different learning rates for the proposed LGL-HCBF method.

1) Learning rates selection: Since the learning rate greatly affects the convergence rate of the proposed LGL-HCBF method, we simulate the influence of different learning rate selections on the convergence rate and the loss. Specifically, it compares the average logarithmic loss obtained as it varies with the episode under different learning rate selections. As shown in Fig. 5, a relatively large learning rate (i.e., 4.5×10^{-2}) results to increased oscillations, with periodic spikes in the logarithmic loss function, which indicates instability in the learning process. On the contrary, a relatively small learning rate (i.e., 4.5×10^{-5} and 4.5×10^{-6}) takes too long to converge. Although the learning rate of 4.5×10^{-3} converges faster than the two mentioned above, it stabilizes at higher logarithmic loss values compared to the setting of 4.5×10^{-4}. Therefore, we adopt a learning rate of 4.5×10^{-4} for the following simulations.

2) Sequential training order design: To avoid training instability or overfitting when handling scenarios with large distribution shifts, the training order should be carefully designed. Since the learning tasks are generated from a continuous mobility process, adjacent scenarios are inherently correlated rather than completely independent. This property enables the sequential arrangement of highly similar tasks, allowing the model to gradually adapt to topology variations and stably capture the characteristics of different scenarios. Therefore, to quantify the similarity between different scenarios, *graph edit distance* (GED) [64] is introduced as the similarity metric. GED quantifies the minimum transformation cost between two graphs by measuring the total cost of edit operations, such as node and edge insertion, deletion, and feature replacement. Specifically, the GED between the dataset $\mathcal{D}_s$ and $\mathcal{D}_{s'}$ is expressed by

$$\mathrm{GED}(\mathcal{D}_s,\mathcal{D}_{s'})=\frac{\sum_{i=1}^{D_s}\sum_{j=1}^{D_{s'}}\varrho(\mathcal{G}_{s,i},\mathcal{G}_{s',j})}{D_s\times D_{s'}},\tag{34}$$

where $\mathcal{G}_{s,i}\in\mathcal{D}_s$, $\mathcal{G}_{s',j}\in\mathcal{D}_{s'}$, and $\varrho(\mathcal{G}_{s,i},\mathcal{G}_{s',j})$ is the editing cost function.

Definition 4: (Editing cost function) The editing cost function is defined as

$$\varrho(\mathcal{G}_{s,i},\mathcal{G}_{s',j})=\frac{A\left(s,s'\right)+A\left(\iota_s,\iota_{s'}\right)+\frac{\sum_{i=1}^{s}\sum_{j=1}^{s'}B\left(\boldsymbol{x}_{s,i},\boldsymbol{x}_{s',j}\right)}{s\times s'}}{3},\tag{35}$$

with $A\left(a,b\right)=\frac{|a-b|}{\max(a,b)}$ and $B\left(a,b\right)=\frac{\mathbf{a}\cdot\mathbf{b}}{\|\mathbf{a}\|\|\mathbf{b}\|}$ being cosine similarity.

According to *Definition 4*, the editing cost function considers both the cost caused by the node or edge insertion/deletion, and feature replacement. The higher the value of the editing cost, the greater the difference between the two graph, and similarly, between the datasets. Thus, the scenario similarity between the dataset $\mathcal{D}_s$ and $\mathcal{D}_{s'}$ is given by

$$\mathrm{Sim}(\mathcal{D}_s,\mathcal{D}_{s'})=1-\mathrm{GED}(\mathcal{D}_s,\mathcal{D}_{s'}).\tag{36}$$

The similarity among the simulated scenarios with different numbers of MVs (i.e., 16, 14, 12, 10, 8, 6, 4, 2) is presented in Table III. Consequently, the proposed LGL-HCBF method is trained incrementally across these scenarios in a sequential manner, following a decreasing order in the number of MVs, i.e., 16 → 14 → 12 → 10 → 8 → 6 → 4 → 2.

TABLE III
The scenario similarity

Training stage	1 → 2	1 → 3	1 → 4	1 → 5	1 → 6	1 → 7	1 → 8
The number of MVs	16 → 14	16 → 12	16 → 10	16 → 8	16 → 6	16 → 4	16 → 2
Scenario diversity	0.844	0.633	0.45	0.294	0.197	0.117	0.055

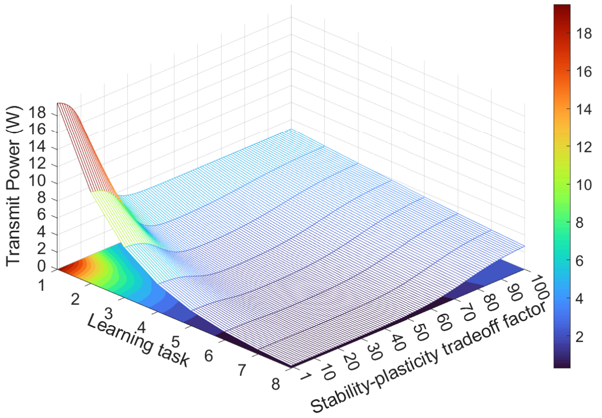

Fig. 6: Transmit power versus different stability-plasticity tradeoff factors.

3) Stability-plasticity tradeoff factor selection: Since the stability-plasticity tradeoff factors significantly impact the ability to integrate new knowledge while preventing the forgetting of previous knowledge, Fig. 6 shows the transmit power at the BS for each learning task, under various stability-plasticity tradeoff factors ξ. As shown in Fig. 6, when the factor is set to a relatively small value, the model tends to overly focus on the performance in its subsequent scenario, leading to catastrophic forgetting of knowledge from previous scenarios. Specifically, when the stability-plasticity tradeoff factor is set to 1, it results in lower transmit power in the 8-th training stage compared to other configurations with relatively larger factors. However, in the previously learned scenarios, the transmit power increases drastically due to catastrophic forgetting. In contrast, when the factor is set to a relatively large value (e.g., 100), the model performs poorly in subsequent scenarios, with higher transmit power, which indicates a weaker ability to adapt to new scenarios. However, in the previous learned scenarios, the model manages to maintain lower transmit power. This suggests that with a larger factor, the model favors the preservation of old knowledge but prevents the rapid learning of new scenarios. Therefore, we adopt a stability-plasticity tradeoff factor $\xi=60$ for the following simulations.

4) Effect of node and edge feature selection on transmit power performance: To verify the impact of feature selection on the transmit power performance, as shown in Fig. 7, we compare the proposed node-edge feature design with three other different feature design schemes, namely, removing node features; using only the channel gain magnitude of imperfect CSI as node features; and removing edge features. Under different MV velocity conditions, the required BS transmit power subject to the QoS constraints is compared across all schemes. It indicates that removing node features causes the transmit power to rise rapidly and quickly drives the system into the infeasible region as the MV velocity increases. The

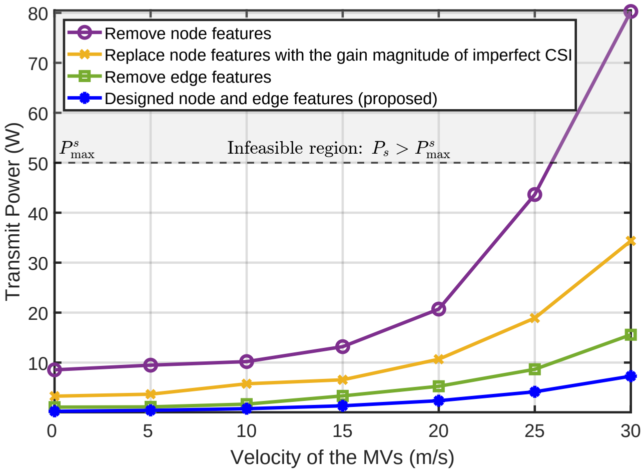

Fig. 7: Transmit power versus velocity of the MVs under different node and edge feature design.

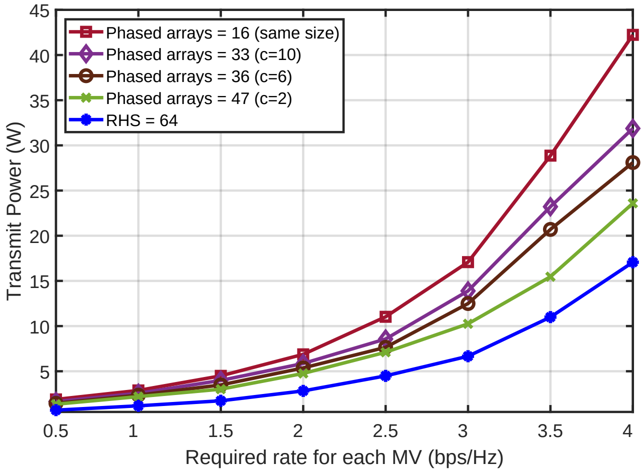

Fig. 8: Transmit power versus required rate for each MV in same size and hardware cost of different type antenna network.

reason is that without CSI-driven node features, the model can hardly distinguish the quality differences among communication links, thereby failing to effectively learn the HCBF strategy. Although using only the channel gain magnitude as the node feature outperforms removing node features, ignoring phase information and richer structural CSI severely limits its capability to characterize multi-user interference coupling, leading to notable performance degradation. Moreover, removing edge features degrades the model performance, as the lack of geometric and topological information hinders accurate modeling of the dynamic interference structure, thereby increasing the transmit power to satisfy QoS constraints. In contrast, the proposed node and edge feature design consistently achieve the lowest transmit power requirement across all velocity ranges. These results demonstrate that feature design has a significant impact on the transmit power, and that the proposed node-edge features enable more accurate characterization of channel conditions and multi-user interference, thereby reducing the transmit power.

C. The Gain Achieved by RHS-based HCBF

1) Comparison of the transmit power under identical size and hardware cost constraints: To show the advantages of the RHS in terms of size and hardware cost, Fig. 8 shows the transmit power at the BS versus the required rate for each MV, i.e., $\tilde{R}^s_l$, and compares the performance of RHS-based HCBF scheme with phased-array beamforming scheme at the identical size and hardware cost. Specifically, for the aspect of size, the element spacing of the phased arrays is typically about half wavelength [65], while for the RHS, it is set to one quarter wavelength [4]. For the aspect of cost, the major cost of a phased array lies in the T/R modules, which account for 53% of the total hardware cost [68]. In contrast, the primary cost of an RHS comes from the metamaterial elements, which are less expensive than T/R modules [69]. The hardware cost of a metamaterial element is denoted by C_0, while the cost of a T/R module is $c \cdot C_0$, and the cost of other components is $\frac{47}{53}c \cdot C_0$, where c represents the cost ratio of a phased array's T/R module to a metamaterial element. In general, c is in the range of 2 to 10 [70]. Therefore, the hardware cost of an RHS with N elements is equivalent to the cost of a phased array with $\frac{53+47c}{100c} \cdot N$ antenna elements.

From Fig. 8, it is observed that when the required data rate is low, the transmit power for both the phased-array beamforming scheme and the RHS-based HCBF scheme, regardless of whether they have the same size or cost, is similar. The reason is that, in low-rate scenarios, despite having fewer antenna elements, phased arrays can still utilize spatial gain to satisfy the rate requirements of MVs with relatively low transmit power. However, as the required rate for each MV increases, the RHS-based HCBF scheme outperforms the phased-array beamforming scheme by achieving the required rate with lower transmit power. This is because the phased arrays, with their limited number of antenna elements, cannot fully exploit spatial gain to meet the increasing rate requirements, and thus have to increase transmit power. Consequently, the superiority of the RHS in terms of size and hardware cost savings becomes more apparent as both the required rate for each MV and the cost ratio increase.

2) Effects of the size of RHS on the transmit power with different amplitude-controlled mode: To illustrate the advantages of the continuous amplitude-controlled mode, Fig. 9 plots the transmit power versus the size of the RHS, M, for different amplitude-controlled modes. It is seen that HCBF with continuous amplitude control achieves lower transmit power at the BS and outperforms both the discrete binary amplitude control and random amplitude control modes. The transmit power decreases rapidly as the RHS size increases, then gradually levels off as the size continues to grow, because the array gain saturates as the size increases further, causing the reduction in transmit power to plateau. This indicates that the RHS

---

[4] According to effective medium theory, increasing the density of RHS elements enlarges the effective aperture and improves radiation performance [66]. However, such gains do not scale linearly with the number of elements, and overly dense deployments exacerbate mutual coupling effects and increase manufacturing complexity. Therefore, by balancing the tradeoff between manufacturing complexity and radiation performance, the element spacing of the RHS is set to one quarter wavelength [67].

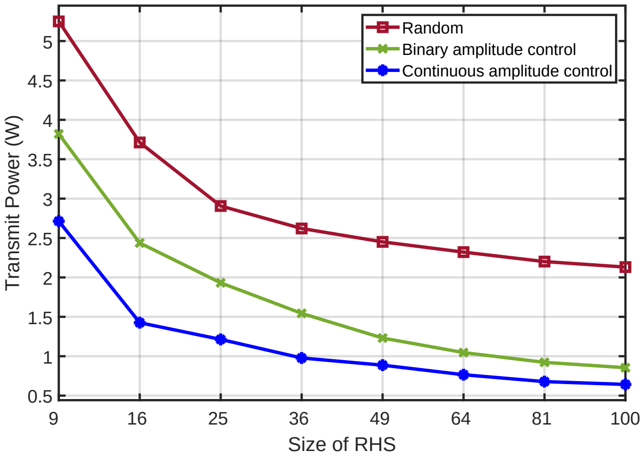

Fig. 9: Transmit power versus the size of the RHS with different amplitude-controlled modes.

does not rely on extremely large-scale elements to achieve significant performance gains [5]. Besides, as the size of the RHS increases, the transmit power gap between the continuous amplitude-controlled RHS and the binary amplitude-controlled RHS gradually narrows. The reason is that, when the RHS size is small, the precision of amplitude control significantly impacts beamforming accuracy. The continuous amplitude-controlled RHS can adjust coefficients more precisely, allowing for better control of beam direction and power distribution, thereby significantly reducing transmit power. In contrast, the binary amplitude-controlled RHS exhibits lower adjustment precision, which limits its performance at small sizes and results in higher transmit power. As the size increases, the binary amplitude-controlled RHS, despite its lower adjustment precision, still benefits from certain multiplexing gains. Once the size reaches a certain threshold, its multiplexing performance approaches that of the continuous amplitude-controlled RHS, causing the transmit power gap to narrow.

D. *Performance of the Proposed LGL-HCBF Method*

To quantify how well the model retains knowledge from previous learning tasks or its learning ability on the current task, a specific metric called the *approximation ratio* is defined. The metric aims to reflect both the performance changes of the updated model on previous learning tasks and its learning ability on the current task, thereby helping identify potential forgetting and non-learnability risks. Based on this, the approximation ratio is defined as the ratio between the model's output on these learning tasks and the optimal performance obtained by the single-scenario re-training (SSRT) method, which serves as the upper bound in our simulation. Specifically, unlike LGL-based methods, which balance between retaining knowledge from previous scenarios and adapting to new ones, the SSRT method involves training the model independently and exclusively for each scenario, initializing the parameters from scratch every time without considering any previous learning tasks. Therefore, the performance achieved by SSRT in each scenario is taken as the theoretical optimum, providing a benchmark to evaluate how closely LGL-based methods can approach single-task optimality. The comparison is divided into two parts: 1) whether the rate requirements of MVs are satisfied, and 2) whether the new model significantly increases transmit power while executing these learning tasks.

Definition 3: (Approximation ratio) The approximation ratio $F_{i\to n}$ for model $\boldsymbol{\Theta}_i$ performed on learning tasks $n \le i$ is expressed as

$$F_{i\to n} = \begin{cases} e^{-\left(\frac{\eta_{i\to n}-1}{\kappa}\right)^2}, & \text{if } \frac{P_{i\to n}}{P_n^*} \le 1, \\ \frac{P_n^*}{P_{i\to n}} \cdot e^{-\left(\frac{\eta_{i\to n}-1}{\kappa}\right)^2}, & \text{if } \frac{P_{i\to n}}{P_n^*} > 1, \end{cases} \tag{37}$$

where $\eta_{i\to n} = \frac{1}{L_n}\sum_{j=1}^{L_n}\frac{R_j^{i\to n}}{R_j^{n,*}}$, L_n is the number of MVs in learning task n, and κ is the hyperparameter that controls the width of the Gaussian function. $R_j^{i\to n}$, $P_{i\to n}$, $R_j^{n,*}$ and P_n^* represent the achievable rate of MVs and transmit power at BS achieved by the model $\boldsymbol{\Theta}_i$ and $\boldsymbol{\Theta}^*_{\mathrm{SSRT},n}$ on the learning task n.

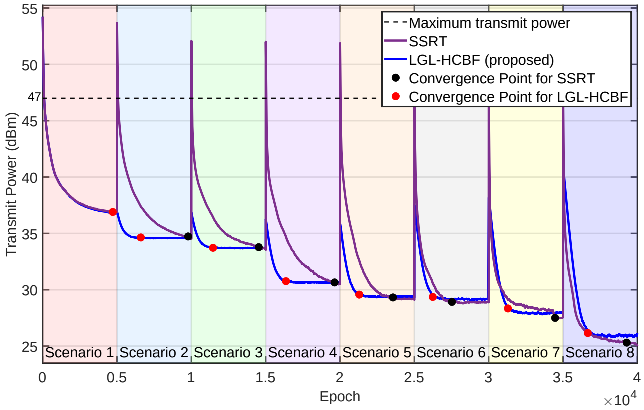

Fig. 10: Transmit power versus different amount of MVs in the varying network topology scenarios.

1) The adaptability performance of the proposed LGL-HCBF: To show the superiority of the proposed LGL-HCBF method in terms of adaptability, Fig. 10 simulates the transmit power at the BS using the proposed method and the SSRT method across different network topology scenarios, ranging from 16 to 2 MV scenarios. The SSRT method cannot leverage any knowledge learned from previous tasks. In Fig. 10, the transmit power at the BS shows a steady decline as the number of MVs decreases for both methods. The performance of the proposed LGL-HCBF method in its first training scenario is comparable to that of the SSRT method, as the model has not yet accumulated prior knowledge, and the data and learning task characteristics are identical in both methods. As subsequent scenarios are introduced, gradually transitioning from more complex scenarios (e.g., 16 MVs) to simpler ones (e.g., 2 MVs), the proposed LGL-HCBF method leverages the knowledge gained from similar scenarios to quickly adapt to subsequent scenarios. This enables the model to achieve faster

---

[5] Although RHS eliminates the power consumption associated with active amplification and complex phase-shifting circuits, the additional power overhead introduced by element biasing and control networks becomes non-negligible in ultra-large-scale RHS deployments [71], thereby reducing the overall energy efficiency gains.

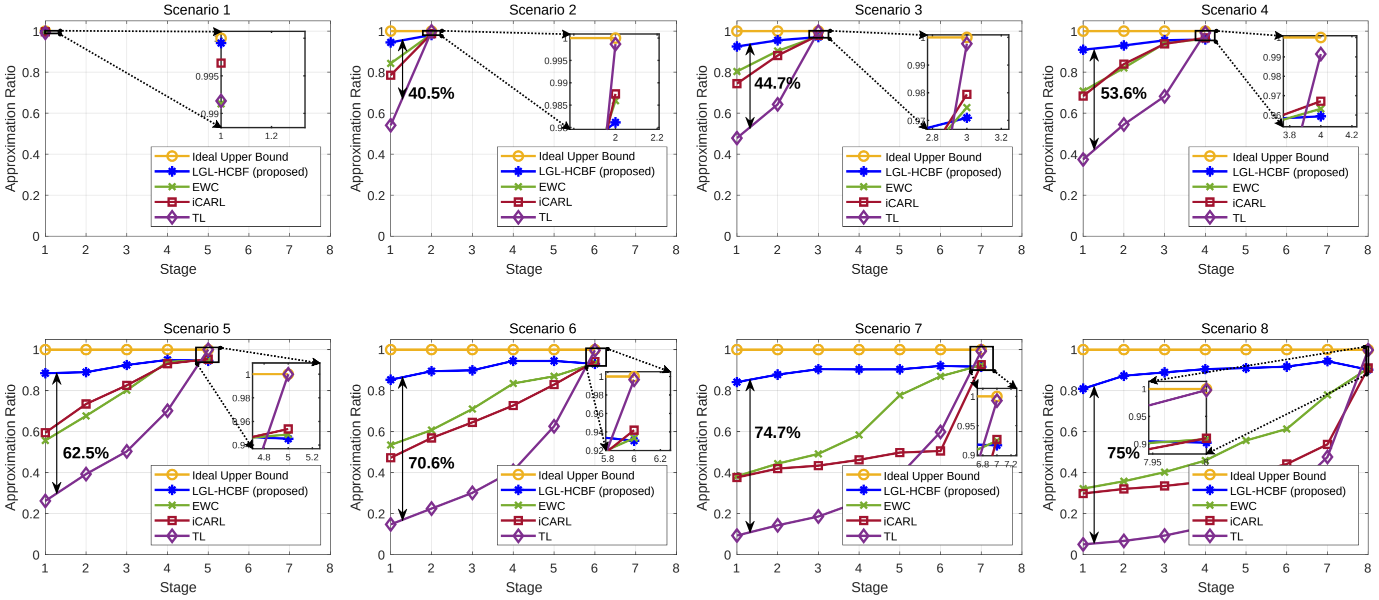

Fig. 11: Evolution of performance for each scenario when gradually adding new scenarios to the model. Different scenarios trained at different training stages are shown in separate sub-graphs.

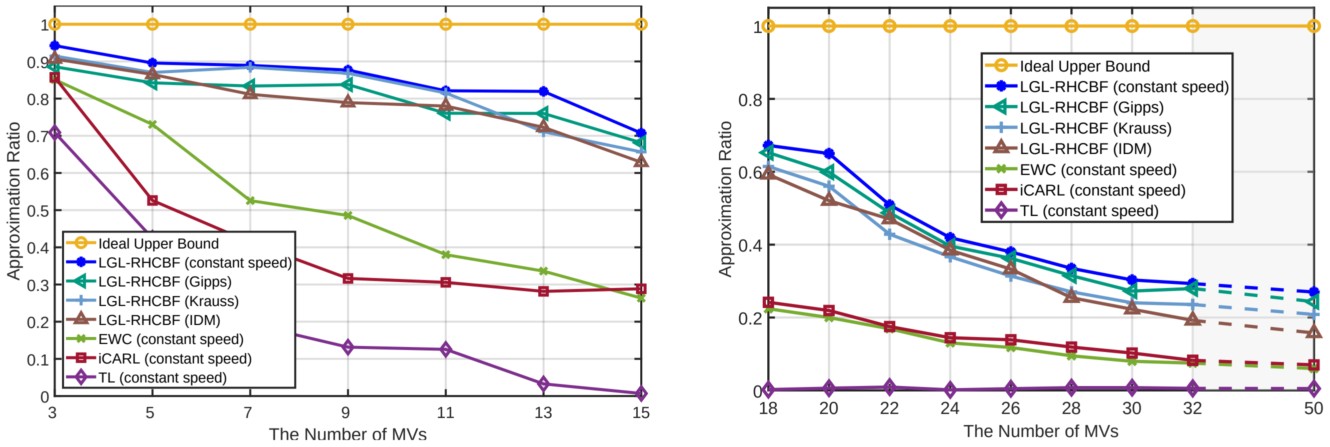

(a) Approximation ratio versus similar scenarios.

(b) Approximation ratio versus expansion scenarios.

Fig. 12: Approximation ratio versus unseen scenarios under different methods

convergence during training and stronger adaptability, thereby reducing the time required for repetitive training.

2) The stability-plasticity performance of the proposed LGL-HCBF: To evaluate the stability and plasticity of the proposed method, which refers to its ability to retain performance from previous scenarios and learning new ones during continual training, Fig. 11 plots the approximation ratio achieved by the proposed LGL-HCBF method, compared with state-of-the-art benchmark methods, namely elastic weight consolidation (EWC), incremental classifier and representation learning (iCARL), and transfer learning (TL), across eight training stages. The results show that the proposed LGL-HCBF method significantly enhances stability throughout the training process with minimal plasticity cost, consistently outperforming the benchmark methods. Specifically, the TL method performs relatively well when learning new scenarios, i.e., high plasticity; however, it suffers from severe catastrophic forgetting. As the training stage progresses, its performance on previously learned scenarios degrades substantially. This is because the core mechanism of TL is model fine-tuning, which adjusts the entire NN to adapt to new scenarios, which gradually forgets knowledge learned from previous ones. Compared to TL, iCARL and EWC perform better, particularly in alleviating forgetting of previous scenarios, but their overall effectiveness remains suboptimal, with forgetting still occurring as training progresses. The approximation ratio achieved by the proposed LGL-HCBF method significantly outperforms that of the baseline methods. As the number of scenarios increases, the anti-forgetting capability of the proposed method becomes increasingly prominent. Compared to TL, the proposed method achieves an approximately 75% improvement in stability with only an 8% plasticity cost. This superior performance stems from two anti-forgetting mechanisms, which enable dynamic adjustment of network weights while preserving knowledge from previous scenarios.

3) The transfer ability of the proposed LGL-HCBF: The transfer ability of the method is crucial for real-world applications, as it is impractical to provide the model with all possible training scenarios. A model with strong transfer ability can leverage knowledge learned from one set of scenarios to generalize to unseen ones, thereby enhancing its generalization in dynamic environments. Fig. 12 shows the transfer performance of the proposed method and several baseline methods in both *similar scenarios* and *expansion scenarios*. During the training stage, the model is trained on scenarios with $\{16, 14, 12, 10, 8, 6, 4, 2\}$ MVs. Subsequently, the trained model is transferred to similar scenarios, which test its ability to generalize to scenarios that are close in structure but differ slightly in terms of the number of MVs. As shown in Fig. 12a, the proposed LGL-HCBF method consistently outperforms the baseline methods in similar scenarios, with the approximation ratio remaining above 0.7. As shown in Fig. 12b, the trained model is transferred to more congested cases with 18 to 50 MVs. As the complexity of the scenarios increases (i.e., more MVs), the similarity to the learned scenarios decreases, leading to a gradual decline in the approximation ratio of the proposed method. This trend shows that the transfer ability of the proposed method weakens as the network topology similarity decreases. Nevertheless, despite this performance degradation, the proposed method consistently outperforms all baseline methods across all expansion scenarios. Besides, to address realistic traffic dynamics beyond constant-speed motion, we also evaluate LGL-HCBF under state-of-the-art mobility models, including Gipps-, Krauss-, and intelligent driver model (IDM)-type car-following behaviors. These results show that the proposed method is insensitive to the mobility model, as it only requires time-indexed MV states generated by the mobility process, such as vehicle positions, topology relations, and the corresponding CSI.

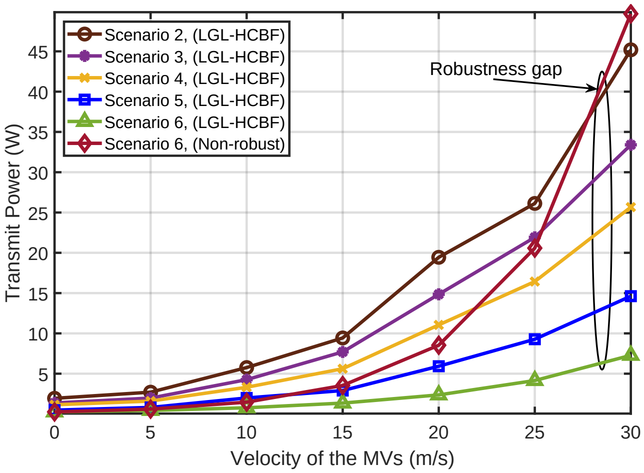

Fig. 13: Transmit power versus velocity of the MVs under different scenarios.

4) The robustness of the proposed LGL-HCBF: To show the robustness of the proposed LGL-HCBF method to CSI uncertainty induced by MV mobility, Fig. 13 simulates the transmit power across various scenarios for different velocities by comparing the robust HCBF scheme based on the proposed method with the non-robust HCBF scheme using the maximum ratio transmission (MRT) method. The DBF and HoBF matrices $\{\boldsymbol{V}_s, \boldsymbol{Q}_s\}$ are constructed using only the estimated CSI, treating the estimated CSI $\left\{\hat{\mathbf{h}}_l^s\left[t - T_d\right]\right\}$ as the true CSI. Fig. 13 shows that the transmit power at the BS increases with vehicle speed for both the robust and non-robust schemes across different scenarios, albeit to different degrees. Specifically, there is a relatively slight rise in terms of transmit power obtained by the proposed LGL-HCBF method, whereas that of the non-robust scheme grows markedly. Moreover, the robustness gap between the non-robust scheme and the proposed LGL-HCBF method widens as MV speed increases, indicating that the non-robust scheme requires significantly more transmit power to meet the rate demands of MVs. This trend can be explained by the impact of MV speed on the temporal correlation coefficient, ρ_l^s. As MV speed increases, ρ_l^s decreases monotonically, thereby rendering the estimated CSI more outdated. In such cases, the non-robust scheme, which relies on outdated CSI, suffers a greater performance loss. To compensate for this loss and ensure reliable transmission, the BS needs to increase transmit power. In contrast, the LGL-HCBF method demonstrates better robustness to these variations and requires less transmit power to maintain performance.

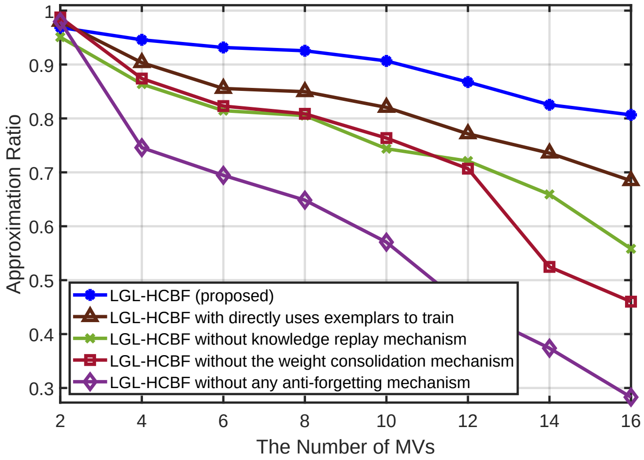

Fig. 14: Effect of the knowledge replay mechanism and the weight consolidation mechanism.

5) Effectiveness of the knowledge replay mechanism and the weight consolidation mechanism: To verify the effectiveness of the knowledge replay mechanism and the weight consolidation mechanism, ablation experiments are designed. As shown in Fig. 14, the proposed LGL-HCBF method exhibits strong anti-forgetting performance across all scenarios, maintaining an approximation ratio consistently above 0.8. Besides, the approximation ratio achieved by the variant that directly uses exemplars for training is approximately 10% lower than that of the proposed LGL-HCBF method. This highlights that the model in our proposed method benefits from soft-labeled exemplars, enabling it to learn the optimal mapping relationship more effectively. Furthermore, the approximation ratio obtained by the proposed LGL-HCBF method without the knowledge replay mechanism is approximately 24% lower than that of the LGL-HCBF method. Moreover, it can be seen that without the weight consolidation mechanism, the approximation ratio experiences the most significant decline, approximately 33%, particularly as the number of scenarios increases, which shows that the weight consolidation mechanism plays a crucial role in the model, as it effectively helps preserve knowledge from earlier scenarios while adapting to new ones. The approximation ratio of the model without any anti-forgetting mechanism drops sharply, especially in the subsequent scenarios, with performance nearing 0.3, which verifies that both mechanisms are essential for preventing catastrophic forgetting in the model.

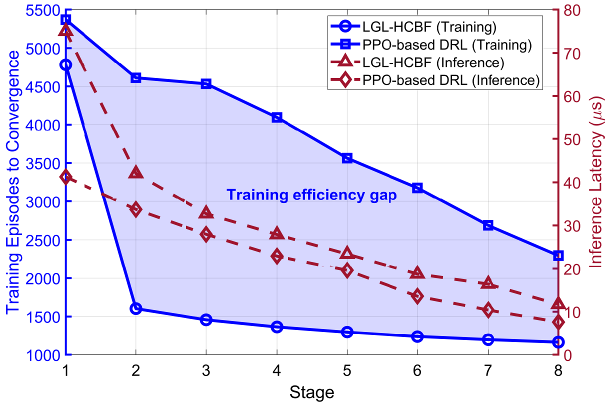

Fig. 15: Comparison of training convergence and inference latency across training stages.

6) Training efficiency and inference latency of the proposed LGL-HCBF: To validate the training efficiency and real-time feasibility of the proposed LGL-HCBF method, Fig. 15 compares the performance of the proposed method with that of traditional proximal policy optimization (PPO)-based DRL method in terms of the number of training episodes required for convergence and the inference latency across training stages. The proposed LGL-HCBF consistently requires far fewer training episodes to converge than the DRL baseline. Although the number of training episodes required by the DRL method decreases across training stages, this reduction is mainly attributable to task simplification resulting from the decrease in the number of connected MVs, i.e., the reduction in the state-action space dimensionality and inter-user interference, rather than any intrinsic improvement of the DRL algorithm itself. In contrast, the convergence acceleration of the proposed LGL-HCBF is not solely attributed to the learning task simplification. Instead, it stems from the lifelong learning design, in which parameter inheritance enables effective reuse of previously acquired knowledge across scenarios, as evidenced by the training efficiency gap across training stages. Moreover, the proposed LGL-HCBF achieves microsecond-level inference latency (below 80 μs), which is shorter than the CSI coherence timescale in high-mobility IoV [72], ensuring that beamforming decisions are generated before the CSI becomes outdated and thereby demonstrating real-time feasibility.

V. CONCLUSION

This paper studied a downlink RHS-aided IoV communication system and proposed an RHS-based HCBF scheme to reduce the system power consumption. Besides, an LGL-HCBF optimization method was proposed to minimize the total transmit power at the BS, with imperfect CSI. To better adapt to changes in IoV network topology, IGCN was employed in the proposed LGL-HCBF method to enable parameter sharing and the exchange of local structural information, without retraining from scratch when the network topology changes. To further overcome the stability-plasticity dilemma, two complementary mechanisms, namely, knowledge replay and weight consolidation, were designed to retain knowledge learned from previous scenarios. Simulation results demonstrated that the proposed method showed faster adaptation, and maintained a higher approximation ratio on previously learned scenarios, outperforming several baseline methods.

REFERENCES

[1] C. Hendrickson *et al.*, “Connected and autonomous vehicles 2040 vision,” *Harrisburg, PA: PennDOT*, 2014.

[2] K. N. Qureshi *et al.*, “Internet of vehicles: Key technologies, network model, solutions and challenges with future aspects,” *IEEE Trans. Intell. Transp. Syst.*, vol. 22, no. 3, pp. 1777–1786, 2020.

[3] B. Ai *et al.*, “5G key technologies for smart railways,” *Proc. IEEE*, vol. 108, no. 6, pp. 856–893, 2020.

[4] ——, “6G-enabled smart railways,” *arXiv preprint arXiv:2505.12946*, 2025.

[5] W. Roh *et al.*, “Millimeter-wave beamforming as an enabling technology for 5G cellular communications: Theoretical feasibility and prototype results,” *IEEE Commun. Mag.*, vol. 52, no. 2, pp. 106–113, 2014.

[6] S. Han *et al.*, “Large-scale antenna systems with hybrid analog and digital beamforming for millimeter wave 5G,” *IEEE Commun. Mag.*, vol. 53, no. 1, pp. 186–194, 2015.

[7] M. Giordani *et al.*, “Millimeter wave communication in vehicular networks: Challenges and opportunities,” in *Proc. MOCAST*, 2017, pp. 1–6.

[8] F. Qamar *et al.*, “Multi-antenna array-based massive MIMO for B5G/6G: State of the art, challenges, and future research directions,” *Information*, vol. 15, no. 8, p. 442, 2024.

[9] D. Wang *et al.*, “An overview of transmission theory and techniques of large-scale antenna systems for 5G wireless communications,” *Sci. China Inf. Sci.*, vol. 59, pp. 1–18, 2016.

[10] W. Jiang, B. Han, M. A. Habibi, and H. D. Schotten, “The road towards 6G: A comprehensive survey,” *IEEE Open J. Commun. Soc*, vol. 2, pp. 334–366, 2021.

[11] S. Lim, C. Caloz, and T. Itoh, “Metamaterial-based electronically controlled transmission-line structure as a novel leaky-wave antenna with tunable radiation angle and beamwidth,” *IEEE Trans. Microw. Theory Techn.*, vol. 52, no. 12, pp. 2678–2690, 2004.

[12] M. Di Renzo *et al.*, “Smart radio environments empowered by reconfigurable intelligent surfaces: How it works, state of research, and the road ahead,” *IEEE J. Sel. Areas Commun.*, vol. 38, no. 11, pp. 2450–2525, 2020.

[13] Q. Wu *et al.*, “Intelligent reflecting surface-aided wireless communications: A tutorial,” *IEEE Trans. Commun.*, vol. 69, no. 5, pp. 3313–3351, 2021.

[14] T. Sleasman *et al.*, “Waveguide-fed tunable metamaterial element for dynamic apertures,” *IEEE Antennas Wirel. Propag*, vol. 15, pp. 606–609, 2016.

[15] R. Deng, Y. Zhang, H. Zhang, B. Di, H. Zhang, and L. Song, “Reconfigurable holographic surface: A new paradigm to implement holographic radio,” *IEEE Veh. Technol. Mag.*, vol. 18, no. 1, pp. 20–28, 2023.

[16] O. Yurduseven *et al.*, “Design and analysis of a reconfigurable holographic metasurface aperture for dynamic focusing in the fresnel zone,” *IEEE Access*, vol. 5, pp. 15 055–15 065, 2017.

[17] B.-J. Che *et al.*, “Reconfigurable holographic antenna with low sidelobe level based on liquid crystals,” *Journal of Physics D: Applied Physics*, vol. 53, no. 31, p. 315302, 2020.

[18] M. C. Johnson *et al.*, "Sidelobe canceling for reconfigurable holographic metamaterial antenna," *IEEE Trans. Antennas Propag.*, vol. 63, no. 4, pp. 1881–1886, 2015.

[19] R. Deng *et al.*, "Reconfigurable holographic surface: Holographic beamforming for metasurface-aided wireless communications," *IEEE Trans. Veh. Technol.*, vol. 70, no. 6, pp. 6255–6259, 2021.

[20] Q. Li *et al.*, "Energy-efficient reconfigurable holographic surfaces operating in the presence of realistic hardware impairments," *IEEE Trans. Commun.*, 2024.

[21] R. Deng *et al.*, "Holographic MIMO for LEO satellite communications aided by reconfigurable holographic surfaces," *IEEE J. Sel. Areas Commun.*, vol. 40, no. 10, pp. 3071–3085, 2022.

[22] D. Geng *et al.*, "Reconfigurable holographic surface-aided distributed edge computing," in *Proc. WCSP*. IEEE, 2023, pp. 1138–1143.

[23] J. Hu *et al.*, "Holofed: Environment-adaptive positioning via multi-band reconfigurable holographic surfaces and federated learning," *IEEE J. Sel. Areas Commun.*, 2023.

[24] X. Zhang *et al.*, "Multi-target detection for reconfigurable holographic surfaces enabled radar," in *Proc. GLOBECOM*. IEEE, 2023, pp. 6634–6639.

[25] ——, "Holographic radar: Target detection enabled by reconfigurable holographic surfaces," *IEEE Commun. Lett.*, vol. 27, no. 1, pp. 332–336, 2022.

[26] T. Wei *et al.*, "RIS-aided wideband DFRC with reconfigurable holographic surface," in *Proc. ICASSP*. IEEE, 2023, pp. 1–5.

[27] J. Wu and P. Fan, "A survey on high mobility wireless communications: Challenges, opportunities and solutions," *IEEE Access*, vol. 4, pp. 450–476, 2016.

[28] K. Moghaddasi *et al.*, "Multi-objective secure task offloading strategy for blockchain-enabled IoV-MEC systems: A Double Deep Q-Network approach," *IEEE Access*, vol. 12, pp. 3437–3463, 2024.

[29] B. Hazarika *et al.*, "DRL-based resource allocation for computation offloading in IoV networks," *IEEE Trans Ind. Informat.*, vol. 18, no. 11, pp. 8027–8038, 2022.

[30] X. Li *et al.*, "Graph neural networks for joint communication and sensing optimization in vehicular networks," *IEEE J. Sel. Areas Commun.*, vol. 41, no. 12, pp. 3893–3907, 2023.

[31] ——, "Joint optimization of sensing and communications in vehicular networks: A graph neural network-based approach," in *Proc. ICC*, 2023, pp. 5719–5724.

[32] ——, "Dynamic graph neural networks for joint Terahertz based sensing and communication optimization in vehicular networks," in *Proc. WCNC*, 2024, pp. 1–6.

[33] ——, "Jointly optimizing Terahertz based sensing and communications in vehicular networks: A dynamic graph neural network approach," *IEEE Trans. Wireless Commun.*, vol. 23, no. 10, pp. 12 917–12 932, 2024.

[34] Z. He *et al.*, "Resource allocation based on graph neural networks in vehicular communications," in *Proc. GLOBECOM*, 2020, pp. 1–5.

[35] C. Wang *et al.*, "Lifelong graph learning," in *Proc. CVPR*, 2022, pp. 13 709–13 718.

[36] Y. Han *et al.*, "Graph neural networks with continual learning for fake news detection from social media," *arXiv preprint arXiv:2007.03316*, 2020.

[37] X. Chen *et al.*, "Trafficstream: A streaming traffic flow forecasting framework based on graph neural networks and continual learning," *Proc. 30th Int. Joint Conf. Artif. Intell.*, 2021.

[38] T. Guo *et al.*, "Graduate employment prediction with bias," in *Proc. AAAI Conf. Artif. Intell.*, vol. 34, no. 01, 2020, pp. 670–677.

[39] B. Di, "Reconfigurable holographic metasurface aided wideband OFDM communications against beam squint," *IEEE Trans. Veh. Technol.*, vol. 70, no. 5, pp. 5099–5103, 2021.

[40] Q. Qin, L. Gui, P. Cheng, and B. Gong, "Time-varying channel estimation for millimeter wave multiuser MIMO systems," *IEEE Trans. Veh. Technol.*, vol. 67, no. 10, pp. 9435–9448, 2018.

[41] I. A. Hemadeh *et al.*, "Millimeter-wave communications: Physical channel models, design considerations, antenna constructions, and link-budget," *IEEE Commun. Surveys Tuts.*, vol. 20, no. 2, pp. 870–913, 2017.

[42] A. M. Sayeed and B. Aazhang, "Joint multipath-Doppler diversity in mobile wireless communications," *IEEE Trans. Commun.*, vol. 47, no. 1, pp. 123–132, 1999.

[43] 3GPP, "Study on channel model for frequencies from 0.5 to 100 GHz," Technical Report TR 38.901, 2020.

[44] Y.-T. Chiew and Y.-P. Lin, "Channel estimation for hybrid mmWave systems using generalized Kronecker compressive sensing (G-KCS) with successive decision-aided recovery," *IEEE Trans. Signal Process*, 2024.

[45] X. Xia *et al.*, "Learning the time-varying massive MIMO channels: Robust estimation and data-aided prediction," *IEEE Trans. Veh. Technol.*, vol. 69, no. 8, pp. 8080–8096, 2020.

[46] L. You *et al.*, "Channel acquisition for massive MIMO-OFDM with adjustable phase shift pilots," *IEEE Trans. Signal Process.*, vol. 64, no. 6, pp. 1461–1476, 2015.

[47] J. Mao *et al.*, "A GAN-based semantic communication for text without CSI," *IEEE Trans. Wireless Commun.*, vol. 23, no. 10, pp. 14 498–14 514, 2024.

[48] Y. Chen *et al.*, "Robust transmission for reconfigurable intelligent surface aided millimeter wave vehicular communications with statistical CSI," *IEEE Trans. Wireless Commun.*, vol. 21, no. 2, pp. 928–944, 2021.

[49] S. S. Haykin, *Digital communications*. Wiley New York, 1988.

[50] Y. Ma *et al.*, "Error performance of transmit beamforming with delayed and limited feedback," *IEEE Trans. Wireless Commun.*, vol. 8, no. 3, pp. 1164–1170, 2009.

[51] C. Meng *et al.*, "Sum-rate maximization in STAR-RIS-assisted RSMA networks: A PPO-based algorithm," *IEEE Internet Things J.*, vol. 11, no. 4, pp. 5667–5680, 2023.

[52] F. G. Febrinanto *et al.*, "Graph lifelong learning: A survey," *IEEE Comput. Intell. Mag.*, vol. 18, no. 1, pp. 32–51, 2023.

[53] X. Wang *et al.*, "A survey on heterogeneous graph embedding: methods, techniques, applications and sources," *IEEE Trans. Big Data*, vol. 9, no. 2, pp. 415–436, 2022.

[54] M. Laal and P. Salamati, "Lifelong learning; why do we need it?" *Procedia-Social and Behavioral Sciences*, vol. 31, pp. 399–403, 2012.

[55] J. Kirkpatrick *et al.*, "Overcoming catastrophic forgetting in neural networks," *Proceedings of the national academy of sciences*, vol. 114, no. 13, pp. 3521–3526, 2017.

[56] B. Wickramasinghe *et al.*, "Continual learning: A review of techniques, challenges, and future directions," *IEEE Trans. Artif. Intell.*, vol. 5, no. 6, pp. 2526–2546, 2024.

[57] L. Galke *et al.*, "Lifelong learning of graph neural networks for open-world node classification," in *Proc. IJCNN*, 2021, pp. 1–8.

[58] T. L. Hayes *et al.*, "Memory efficient experience replay for streaming learning," in *Proc. ICRA*. IEEE, 2019, pp. 9769–9776.

[59] S.-A. Rebuffi *et al.*, "icarl Incremental classifier and representation learning," in *Proc. IEEE Conf. Comput. Vis. Pattern Recog.*, 2017, pp. 2001–2010.

[60] United Nations Economic and Social Commission for Asia and the Pacific, *Asian Highway Handbook*. UN ESCAP, 2003.

[61] T. R. Board, E. National Academies of Sciences, and Medicine, *Highway Capacity Manual 7th Edition: A Guide for Multimodal Mobility Analysis*. Washington, DC: The National Academies Press, 2022.

[62] 3GPP, "Study on evaluation methodology of new vehicle-to-everything (V2X) use cases for LTE and NR," Technical Report TR 37.885, 2019.

[63] R. Deng *et al.*, "Holographic MIMO for LEO satellite communications aided by reconfigurable holographic surfaces," *IEEE J. Sel. Areas Commun.*, vol. 40, no. 10, pp. 3071–3085, 2022.

[64] X. Gao *et al.*, "A survey of graph edit distance," *Pattern Analysis and applications*, vol. 13, pp. 113–129, 2010.

[65] F. Sohrabi and W. Yu, "Hybrid digital and analog beamforming design for large-scale antenna arrays," *IEEE J. Sel. Topics Signal Process.*, vol. 10, no. 3, pp. 501–513, 2016.

[66] R. Liu *et al.*, "Description and explanation of electromagnetic behaviors in artificial metamaterials based on effective medium theory," *Phys. Rev. E, Stat. Phys. Plasmas Fluids Relat. Interdiscip. Top.*, vol. 76, no. 2, p. 026606, 2007.

[67] R. Deng *et al.*, "Reconfigurable holographic surface-enabled multi-user wireless communications: Amplitude-controlled holographic beamforming," *IEEE Trans. Wireless Commun.*, vol. 21, no. 8, pp. 6003–6017, 2022.

[68] J. S. Herd *et al.*, "The evolution to modern phased array architectures," *Proc. IEEE*, vol. 104, no. 3, pp. 519–529, 2015.

[69] T. Gric *et al.*, "Metamaterials: A review from the perspectives of the effective properties and applications," in *in Proc. AES 2024*. Sapienza Università di Roma, 2024, pp. 178–183.

[70] P. Staff, "Holographic beam forming and phased arrays," *Pivotal Commware, Inc., Kirkland, WA, USA*, pp. 68–73, 2019.

[71] B. Di *et al.*, "Reconfigurable holographic surface: A new paradigm for ultra-massive MIMO," *IEEE Trans. Cogn. Commun. Netw.*, vol. 11, no. 6, pp. 3761–3783, 2025.

[72] G. Gharsallah and G. Kaddoum, "Multimodal collaborative perception for dynamic channel prediction in 6G V2X networks," *IEEE Trans. Mach. Learn. Commun. Netw.*, 2025.

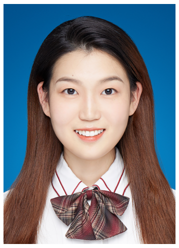

Chanyuan Meng received the B.E. degree from the Beijing-Dublin International College, Beijing University of Technology, Beijing, China, in 2020. She is currently pursuing the Ph.D. degree with the School of Computer Science and Technology, Beijing Jiaotong University, Beijing, China.

Her current research interests include reconfigurable intelligent surface, Internet of Things, and machine learning technologies for wireless communications.

Ke Xiong (Member, IEEE) received the B.S. and Ph.D. degrees from Beijing Jiaotong University (BJTU), Beijing, China, in 2004 and 2010, respectively.

From April 2010 to February 2013, he was a Postdoctoral Research Fellow with the Department of Electronics Engineering, Tsinghua University, Beijing. Since March 2013, he has been a Lecturer, an Associate Professor of BJTU, where he is currently a Full Professor and the Vice Dean of the School of Computer and Information Technology. From September 2015 to September 2016, he was a Visiting Scholar with the University of Maryland, College Park, MD, USA. He has published more than 100 academic papers in referred journals and conferences. His current research interests include wireless cooperative networks, wireless powered networks, and network information theory.

He is a member of China Computer Federation (CCF) and also a senior member of the Chinese Institute of Electronics (CIE) and the Chinese Association for Artificial Intelligence (CAAI). He serves as the Associate Editor-in Chief for the *Chinese Journal New Industrialization Strategy*, and an Editor of Computer Engineering and Software. In 2017, he serves as the leading Editor for the Special Issue Recent Advances in Wireless Powered Communication Networks for *EURASIP Journal on Wireless Communications and Networking* and the Guest Editor of the Special Issue Recent Advances in Cloud-Aware Mobile Fog Computing for *Wireless Communications and Mobile Computing*.

He also served as the Session Chair for IEEE GLOBECOM'2012, IET ICWMMN'2013, IEEE ICC'2013, ACM MOMM'2014, and the Publicity and the Publication Chair for IEEE HMWC'2014, as well as the TPC Co-Chair for IET ICWMMN'2017 and IET ICWMMN'2019. He won the best student paper awards of the HWMC'2014, the best student paper awards of the 25th and 26th Annual Conference of Information Theory of CIT (CIT-IT), the IEEE ICC'2020 and f the HWMC'2014, the best student paper awards of the 25th and 26th Annual Conference of Information Theory of CIT (CIT-IT), the IEEE ICC'2020, the TAOS Technical Committee at IEEE ICC'2020, IEEE ICSTSN'2023, IEEE ICCCS'2023, and also IEEE ICCCS'2024.

Bo Gao (Member, IEEE) received the Ph.D. degree in computer engineering from Virginia Tech, Blacksburg, VA, USA, in 2014.

He was an Assistant Professor with the Institute of Computing Technology, Chinese Academy of Sciences, Beijing, China, from 2014 to 2017. He was a Visiting Researcher with the School of Computing and Communications, Lancaster University, Lancaster, U.K., from 2018 to 2019. He is currently an Associate Professor with the School of Computer and Information Technology, Beijing Jiaotong University, Beijing. He has directed a number of research projects supported by the National Natural Science Foundation of China or other funding agencies. His research interests include wireless networking, dynamic spectrum sharing, mobile-edge computing, and multiagent systems.

Dr. Gao is a member of ACM.

Qiang Ni (Senior Member, IEEE) is currently a Professor and the Head of the Communication Systems Group, School of Computing and Communications, Lancaster University, Lancaster, U.K. His current research interests include future-generation communications and networking, including green communications and networking, millimeter-wave wireless communications, cognitive radio network systems, non-orthogonal multiple access (NOMA), heterogeneous networks, 5G and 6G, SDN, cloud networks, energy harvesting, wireless information and power transfer, the IoT, cyber-physical systems, AI and machine learning, big data analytics, and vehicular networks. He has authored or coauthored more than 300 articles in these areas. He was an IEEE 802.11 Wireless Standard Working Group Voting Member and a contributor to various IEEE wireless standards.

Pingyi Fan (Senior Member, IEEE) received the B.S and M.S. degrees from the Department of Mathematics of Hebei University in 1985 and Nankai University in 1990, respectively, received the Ph.D. degree at the Department of Electronic Engineering of Tsinghua University in 1994.

From Aug. 1997 to March. 1998, he visited Hong Kong University of Science and Technology as Research Associate. From May. 1998 to Oct. 1999, he visited University of Delaware, USA, as research fellow. In March. 2005, he visited NICT of Japan as visiting Professor. From June. 2005 to May 2014, he visited Hong Kong University of Science and Technology for many times and from July 2011 to Sept. 2011, he was a visiting professor of Institute of Network Coding, Chinese University of Hong Kong. He is currently a professor and the director of open source data recognition innovation center, Department of Electronic Engineering, Tsinghua University. His main research interests include B5G technology in wireless communications such as MIMO, OFDMA, Network coding, Network information theory, Machine learning and Big data analysis.

Dr. Fan has obtained many research grants, including national 973 Project, 863 Project, mobile special project and the key R&D program, national natural funds and international cooperation projects. He has published more than 500 papers including 160 IEEE journals and more than 10 ESI highly cited papers as well as 4 academic books. He also applied for more than 40 national invention patents, 7 international patents. He won 10 best paper awards of IEEE international conferences, including IEEE ICCCS2023 and 2024, ICC2020 and Globecom 2014, and received the best paper award of IEEE TAOS Technical Committee in 2020, the excellent editor award of IEEE TWC (2009), the most popular scholar award 2023 of AEIC, the second natural Prize of CIC (2023) and several international innovation exhibition medals, i.e. Gold Medal at the Russian Invention Exhibition-2024, Silver Medal at Geneva Invention Exhibition-2023, and Silver Medal at Paris Invention Exhibition-2023 etc.

Dr. Fan is a Fellow of IET and an Overseas Member of IEICE. He has attended to organize many international conferences including more than 30 times as the General chair/ TCP chair/ Keynote speakers and TPC member of IEEE ICC, Globecom, WCNC, VTC, Inforcom etc. He has served as an Editor for IEEE TRANSACTIONS ON WIRELESS COMMUNICATIONS, Journal of Wireless Communication and Mobile Computing (Wiley), Entrppy (MDPI) and Electronics (MDPI) etc. He is also an Associate Editor of IEEE Transactions on Cognitive Communications and Networking (TCCN), the advisory board member of Inderscienc International Journal of Ad Hoc and Ubiquitous Comuputing, the editorial board member of Open Journal of Mathematical Sciences and IAES international journal of artificial intelligence, the deputy director of China Information Theory society, the Co-chair of China's 6G-ANA TG4, and the Chair of Network and Communication Technology Committee of IEEE ChinaSIP.

Derrick Wing Kwan Ng (S'06-M'12-SM'17-F'21) received his bachelor's degree (with first-class Honors) and the Master of Philosophy degree in electronic engineering from The Hong Kong University of Science and Technology (HKUST), Hong Kong, in 2006 and 2008, respectively, and his Ph.D. degree from The University of British Columbia, Vancouver, BC, Canada, in November 2012. Following his Ph.D., he was a senior postdoctoral fellow at the Institute for Digital Communications, Friedrich-Alexander-University Erlangen-Nürnberg (FAU), Germany. He is currently a Scientia Associate Professor with the University of New South Wales, Sydney, NSW, Australia. His research interests include global optimization, integrated sensing and communication (ISAC), physical layer security, IRS-assisted communication, UAV-assisted communication, wireless information and power transfer, and green (energy-efficient) wireless communications.

He has been recognized as a Highly Cited Researcher by Clarivate Analytics (Web of Science) since 2018 and was named an IEEE Communications Society Distinguished Lecturer for 2026. He was the recipient of the Australian Research Council (ARC) Discovery Early Career Researcher Award 2017, IEEE Communications Society Leonard G. Abraham Prize 2023, IEEE Communications Society Stephen O. Rice Prize 2022, Best Paper Awards at the WCSP 2020, 2021, IEEE TCGCC Best Journal Paper Award 2018, INISCOM 2018, IEEE International Conference on Communications (ICC) 2018, 2021, 2023, 2024, IEEE International Conference on Computing, Networking and Communications (ICNC) 2016, IEEE Wireless Communications and Networking Conference (WCNC) 2012, IEEE Global Telecommunication Conference (Globecom) 2011, 2021, 2023, 2025, and IEEE Third International Conference on Communications and Networking in China 2008. From January 2012 to December 2019, he served as an Editorial Assistant to the Editor-in-Chief of the IEEE Transactions on Communications. He is also an Area Editor of the IEEE Transactions on Communications, an Associate Editor-in-Chief of the IEEE Open Journal of the Communications Society, a member of the IEEE Transactions on Wireless Communications executive editorial committee, and a member of the IEEE Communications Society Fellow Evaluating Committee (2026–2028).

Bo Ai (Fellow, IEEE) received the M.S. and Ph.D. degrees from Xidian University, Xi'an, China, in 2002 and 2004, respectively. He was with Tsinghua University, Beijing, China, where he was an Excellent Postdoctoral Research Fellow in 2007. He is currently a Professor and an Advisor of Ph.D. candidates with Beijing Jiaotong University, Beijing, where he is also the Deputy Director of the State Key Laboratory of Rail Traffic Control and Safety. He is also currently with the Engineering College, Armed Police Force, Xian. He has authored or coauthored six books and 270 scientific research papers, and holds 26 invention patents in his research areas. His interests include the research and applications of orthogonal frequency-division multiplexing techniques, high-power amplifier linearization techniques, radio propagation and channel modeling, global systems for mobile communications for railway systems, and long-term evolution for railway systems.

Dr. Ai is a Fellow of The Institution of Engineering and Technology. He was as a Co-chair or a Session/Track Chair for many international conferences such as the 9th International Heavy Haul Conference (2009); the 2011 IEEE International Conference on Intelligent Rail Transportation; HSRCom2011; the 2012 IEEE International Symposium on Consumer Electronics; the 2013 International Conference on Wireless, Mobile and Multimedia; IEEE Green HetNet 2013; and the IEEE 78th Vehicular Technology Conference (2014). He is an Associate Editor of IEEE TRANSACTIONS ON CONSUMER ELECTRONICS and an Editorial Committee Member of the Wireless Personal Communications journal. He has received many awards such as the Qiushi Outstanding Youth Award by HongKong Qiushi Foundation, the New Century Talents by the Chinese Ministry of Education, the Zhan Tianyou Railway Science and Technology Award by the Chinese Ministry of Railways, and the Science and Technology New Star by the Beijing Municipal Science and Technology Commission.

Khaled Ben Letaief (Fellow, IEEE) received the B.S. (Hons.), M.S., and Ph.D. degrees in electrical engineering from Purdue University, West Lafayette, IN, USA, in 1984, 1986, and 1990, respectively.

From 1990 to 1993, he was a Faculty Member with the University of Melbourne, Melbourne, VIC, Australia. Since 1993, he has been with The Hong Kong University of Science and Technology (HKUST). While at HKUST, he has held many administrative positions, including the Head of the Department of Electronic and Computer Engineering, the Director of the Wireless IC Design Center, the Founding Director of the Huawei Innovation Laboratory, and the Director of Hong Kong Telecom Institute of Information Technology. He was a Chair Professor and the Dean of Engineering. Under his leadership, the School of Engineering transformed its education and research scope, produced high-caliber scholarship, and actively pursued knowledge transfer and societal engagement, achieving significant advances in international rankings (rising from November 2009 to November 2015 according to the QS World University Rankings). From 2015 to 2018, he joined Hamad Bin Khalifa University (HBKU) as a Provost to help establish a research-intensive university in Qatar in partnership with strategic institutions, including Northwestern University, Carnegie Mellon University, Cornell University, and Texas A&M University. He has worked as a Consultant for various organizations, including Huawei, ASTRI, ZTE, Nortel, PricewaterhouseCoopers, and Motorola. He is with the Peng Cheng Laboratory, Shenzhen, China. He is the Internationally Recognized Leader in wireless communications and networks, with research interests in artificial intelligence, big data analytics systems, mobile cloud and edge computing, tactile internet, and 5G systems. His prolific contributions include over 750 publications, which have garnered more than 58 150 citations with a H-index of 105. He holds 15 inventions, including 11 U.S. patents.

Dr. Letaief is a member of the United States National Academy of Engineering, a fellow of Hong Kong Institution of Engineers, and a member of Hong Kong Academy of Engineering Sciences. He has received numerous prestigious awards, including the 2019 Distinguished Research Excellence Award from the School of Engineering, HKUST, the 2019 IEEE Communications Society and Information Theory Society Joint Paper Award, the 2018 IEEE Signal Processing Society Young Author Best Paper Award, the 2017 IEEE Cognitive Networks Technical Committee Publication Award, the 2016 IEEE Signal Processing Society Young Author Best Paper Award, the 2016 IEEE Marconi Prize Paper Award in Wireless Communications, the 2011 IEEE Wireless Communications Technical Committee Recognition Award, the 2011 IEEE Communications Society Harold Sobol Award, the 2010 Purdue University Outstanding Electrical and Computer Engineer Award, the 2009 IEEE Marconi Prize Award in Wireless Communications, the 2007 IEEE Communications Society Joseph LoCicero Publications Exemplary Award, and more than 16 IEEE best paper awards. He is well recognized for his service to IEEE and professional societies, where he has held numerous leadership positions, including a Treasurer of the IEEE Communications Society, the vice president for conferences, the vice president for technical activities, the Chair of the IEEE Committee on Wireless Communications, and an Elected Member of the IEEE Product Services and Publications Board. He is the Founding Editor-in-Chief of IEEE Transactions on Wireless Communications and has served on the editorial boards of other premier journals, including IEEE Journal on Selected Areas in Communications Special Issue on Wireless Communications Series as the Editor-in-Chief. He also served as the President of the IEEE Communications Society from 2018 to 2019. He is recognized by Thomson Reuters as an ISI Highly Cited Researcher and was listed among the top 30 scholars in the AI 2000 Internet of Things category in 2020.